

POLITECNICO DI TORINO

Corso di Laurea Magistrale

in Ingegneria Meccanica

Tesi di Laurea Magistrale

Modelling and simulation of a load handling device for little load carriers with an integrated alignment mechanism



Relatori:

prof. Massimo Sorli
prof. Tommi Kivelä
prof. Steffen Bolender

Candidato:

Massimo Sirigu

Anno accademico 2020/2021

Aknowledgements

I would like to thank my thesis supervisors for the great help they have given me during the months of study in Karlsruhe. I really appreciated the support of the project collaborators at the institute.

Un grazie va soprattutto ai miei genitori e ai miei fratelli Roberto e Antonello, che hanno sempre sostenuto il mio studio, a Cagliari, a Torino, in Germania. Sono felice di poter rendere omaggio ai tanti anni di supporto con il raggiungimento della laurea.

Vorrei infine dedicare un ultimo ringraziamento ai miei colleghi con cui abbiamo passato tanto tempo assieme durante gli studi universitari, ovunque mi trovassi.

Abstract

Massimo Sirigu

Modelling and simulation of a load handling device for little load carriers with an integrated alignment mechanism

The subject of the thesis is the study of a device that allows the automation of the stacking process of load carriers or pallet cages using a pre-existing bridge crane. The load handling device is designed to be easily assembled and disassembled on the crane hook. Usage of a pre-existing bridge crane reduces the investment costs compared to building new automated stacking systems. The main goal of the thesis is to create virtual models of the load handling device concepts and simulate their dynamic performance.

A prototype was built in previous works on this theme. The prototype uses a reaction wheel oriented on the vertical axis to control the yaw movement and a mobile counterweight to balance non-uniform loads. The device uses MEMS gyroscopes and a camera as position sensors to orient and align itself to the box. Experimental tests on the prototype have been carried out for the validation of mathematical equations and the parameters estimation.

New features have been studied to increase the stability of the device and the positioning accuracy of the payload. These features are based on the use of reaction wheels, control moment gyroscopes and movable counterweights to move and balance the payload. A simplified workflow has been designed to carry out picking, conveying and stacking operations.

Table of contents

Acknowledgements	i
Abstract	iii
List of abbreviations	vii
Introduction	9
1.1. Goal setting.....	9
1.2. Structure of the work.....	11
2 Basics	13
2.1. Material handling in warehouses	13
2.2. Inertial measurements	15
2.2.1. MEMS gyroscopes.....	17
2.2.2. Sensor fusion and Kalman filters.....	19
2.3. Simulation environment.....	20
2.3.1. Simscape Multibody.....	21
2.3.2. Stateflow.....	22
3 Prototypes description	23
3.1. First design.....	23
3.2. Second design.....	25
3.2.1. Actuation system.....	26
3.2.2. Balancing system	27
3.2.3. Gripper mechanism.....	27
3.2.4. Sensor system.....	28
3.2.5. Control system	28
4 Experimental tests	29
4.1. Mathematical model.....	29
4.2. Test description	30
4.3. Test results.....	31
5 Vertical axis motion simulation	33
5.1. Actuation system modelling.....	33
5.2. Inertia and friction evaluation	35

5.3. Chain behaviour	37
6 Control design	39
6.1. Description.....	39
6.2. Results.....	40
6.3. Conclusion.....	44
7 KLT gripping process simulation	46
7.1. Simscape model description	46
7.1.1. crane bridge	47
7.1.2. Load handling device.....	48
7.1.3. Contact forces	49
7.1.4. Control logic.....	49
7.2. Simulation results	52
7.2.1. Dynamics.....	52
7.2.2. Balance	53
7.3. Discussion of results.....	54
8 Swing suppression methods	55
8.1. Trolley acceleration control.....	56
8.2. Lateral reaction wheel.....	57
8.3. single pendulum with gyroscope.....	62
8.4. Double pendulum with gyroscope	67
9 Positioning accuracy improvements	69
9.1. Dynamics.....	69
9.2. Balancing operation	71
9.3. tilt angle compensation.....	71
10 Stacking process simulation with a new prototype	77
10.1. Description of work.....	77
10.2. Results	81
11 Conclusion and outlook	83
11.1. Results discussion.....	83
11.2. Prospect of use	84
bibliography	87

List of abbreviations

LHD Load handling device

KLT Kleinladungsträger (Little load carrier)

RW reaction wheel

IMU Inertial measurement unit

MEMS Micro-electromechanical systems

CoM Centre of mass

PID Proportional-Integral-Derivative

VDA Verband der Automobilindustrie (German association of automotive industry)

IFL Institut für Fördertechnik und Logistiksysteme (Institute for material handling and logistics systems)

Introduction

Cranes are widely used in the manufacturing industry. Their structure is designed for the maintenance of suspended objects or for the movement of goods and equipment within the plant. The use of this tool in many working contexts is sporadic, limited to a few transfers per day.

For this reason, the institute of material and logistics decided to use the crane downtime for the automatic storage of load carriers. In article (Bolender, et al. 2018) a new concept is presented. A new trolley with 4 chain hoists is designed to be mounted on the existing bridge. this method involves the automation of pallet cage storage (with base area 800x1200 mm and maximum load weight 800 kg), self-supporting without additional structures. Such system prevents storage from being carried out by manual forklifts which require ample room for manoeuvre.

This system does not allow the rotation of the box. A parallel study (Seifert 2019) introduced the possibility of rotary movement along the vertical axis of the load handling device, mounting it on a single rope hoist and inserting a reaction wheel inside the frame. motion control is entrusted to the IMU and a camera with an image recognition algorithm.

A subsequent study (Fischer 2019) introduces a mechanism for balancing the tilt angle in the case of the centre of mass does not coincide with the geometric centre.

1.1. Goal setting

The core of the thesis is the simulation of the functioning of the LHD. The LHD in question is designed for the storage of small standardized load carriers (R-LKT and C-LKT VDA 4500 series) with grooved bottom for stable and safe self-supporting storage of boxes also with different orientation and dimensions. In conclusion, some considerations are discussed for the scalability of its components for use for pallet cages.

The device is mounted on the crane hook. The motors moving the bridge, trolley and winch are modified for the implementation of automatic control. inverters for the motors (generally three-phase asynchronous motors) and a program that manages torque and speed control are installed.

The work consists of two main parts: the first part is dedicated to the modelling and functioning of the prototype in IFL. It is carried out by conducting tests to estimate the parameters. These parameters will then be used to simulate the complete model for the storage operation.



Figure 1.1: KLT stack on a euro-pallet 800x1200 mm (Koether 2018)

The second part concerns the simulation of new features to increase the dynamic performance of the model and positioning accuracy.

For the study of these features some constraints must be respected:

- the LHD must be assembled and disassembled on the crane hook quickly and easily (for example hanging directly on the crane hook).
- the crane structure must not be changed.
- there can be no interaction between LHD and the surrounding environment (such as external aid structures).

The study therefore falls into the reaction wheels, gyroscope moments, movable counterweights. The principle of these systems lies in the fact that these forces are not counterbalanced by ground reactive forces but are counteracted by the inertia force of other rigid bodies, gyroscopic moments, gravity force.

The IMU is the most suitable sensor for controlling forces, thanks to the fact that it can directly measure the accelerations and speeds along the 3 inertial axes.

The final results to be obtained are:

- obtain a qualitative description of the operation of the LHD by viewing the storage operations.
- identify a possible workflow and outline the weak points.
- verify the theoretical functioning of the new features implemented.

In the conclusion the results will be resumed and the usefulness of the device will be discussed.

1.2. Structure of the work

Chapter 2 introduces the tools covered in the thesis. The first glance is dedicated to the handling of materials in the manufacturing industry, which represents one of the main markets that requires flexible storage of medium and large load carriers. A brief description also covers cranes.

A paragraph is dedicated to MEMS gyroscopes, since it is the main tool of experimental tests and their functioning is not trivial. The concept of sensor fusion and the software used for simulations are also explained.

Chapter 3 describes the state of the art of the device under analysis and the work previously carried out at the IFL. The chapter describes the testbench on which the measurements are carried out.

Chapters 4 and 5 show the conduct and results of the experimental tests. Measurements are performed with the use of MEMS gyroscopes and Hall sensors. The purpose of the measurements is to obtain the simulation parameters inherent in the use of the reaction wheel for the movement of the vertical axis of the device.

The workflow is carried out as follows:

- description of the mathematical equation of the physical phenomenon.
- description of tests conduction.
- exposition and discussion of the measurements obtained.
- description of the block diagram of the simulation.
- comparison between experimental and simulated data.

In Chapter 6 a PID controller is tested to manage the rotation of the device.

It also refers to a workflow of the type:

- mathematical description of the PID control.
- presentation of experimental results and comparison with simulated data.

At the end of the chapter, there is a conclusion that summarizes all the parameters and useful information collected.

Chapter 7 describes the simulation that uses the device in the application context. changes were introduced in the parameters collected in the previous chapters as the original parameters were unsuitable for operation and explanations for the change were introduced.

Chapter 7 ends with the qualitative description of the process showing the characters to be improved on the device.

Chapter 8 shows some design concepts that can be introduced to eliminate the problem of oscillations, such as the movement of the trolley, reaction wheels oriented sideways and the use of gyroscopic couples.

Chapter 9 instead shows new features to increase the positioning accuracy of the box by using the frame mass as a counterweight.

Chapter 10 combines the new features described in the previous chapters together using the same working scheme of chapter 6 showing the theoretical result of the simulations.

The conclusion ends the thesis work with some final considerations on the work done and possible future work.

2 Basics

2.1. Material handling in warehouses

Standardized load carriers are meant to form uniform logistics units and aid for transport, storage, and loading of freight. They create conditions for mechanization and automation in the flow of materials and goods. They are distinguished in base of dimensions: small, medium and large load carriers.

An example of standardisation of small load carriers is made by the recommendations of German association of automotive industry (VDA) (Martin 2016). The dimensions of the boxes are modular and designed for storage on Euro pallets. They have reinforcing ribs, multiple gripping points for manual and automatic use.

In the thesis, R-KLT with dimensions 600x400x280 mm was taken as reference for the load carrier. It has a weight of 3 kg and can load up to 50 kg.



Figure 2. 1. KLT according to recommendations VDA 4500. From left: R-KLT with partially grooved floor, RL-KLT with smooth floor, C-KLT with grooved floor and double reinforced wall (web source: utzgroup.ch).

Table 2.1: types of KLT. the possible dimensions of the box are given by the base area for the 4 possible heights (web source: utzgroup.ch).

Area base	600x400 mm	400x300 mm		
height	147 mm	174 mm	213 mm	280 mm

The storage of the boxes inside the warehouse can take place in different ways.

Pallets are one of the most used tools for stacking. The advantages of using pallets are modularity, stability, ease of handling using forklifts. Above them modular boxes such as KLT can be assembled or load carriers of their size can be positioned. Pallets can be

positioned on the floor with the advantage of being cheap, flexible and allow high density storage with minimum initial investments. The main disadvantages relate to the difficult automation, limited height of stack, and only the box on the top is accessible. the system is mainly used for stacking large quantities of the same product with LIFO storage system (last in first out).

The automatic movement of goods in the warehouse takes place with different methods: the most common are conveyor belts, robotic arms, trolleys on monorails, stacker cranes, up to more complex systems such as self-driving vehicles. For example, conveyor belts guarantee a continuous flow of goods with a low operating cost, but a complex and flexible handling requires a large volume of space and high installation costs. Robotic arms are very flexible but have a limited field of action. Self-driving vehicles have different navigation systems which characterize their freedom of movement, but in general they have great flexibility of use with a limited speed. Each of these systems can be combined to obtain the optimal handling.



Figure 2. 2: examples of automated systems for storage of medium sized loads in pallet racking. Left: stacker crane (Martin 2016). Right: automatic guided forklift (AGV market insights 2019)

Cranes are also a tool that can be used for storage, although they are generally not automated. they have a very large working area and access the load in a vertical direction. There are various types of construction: the bridge cranes, in which the movements follow Cartesian axes; the bridge that supports the winch moves along the beams; the gantry cranes are distinguished by the fact that the winch is mounted on a portal moving on rails or on wheels; very long strokes can be achieved. Jib cranes consist of a central column (or a revolute joint fixed to the wall) and the Jib on which the hoist is mounted. They move along cylindrical coordinates. They are most used for individual workstations because of their limited workspace (max 6 metres of radius).

Bridge cranes can be built with a single beam, where the winch moves in the lower part of the beam, and with a double beam, where the winch moves above the beams, thus allowing both greater resistance and a higher lifting height.

The winch consists of a coil on which the chain or metal wire is rolled, the electric motor and the reducer, and aids for the correct unwinding of the rope or chain. Usually the chain is used for light duty (under 7-8 tons) and they are cheaper the chain also guarantees an exact vertical position, without lateral oscillations, as happens for ropes, which instead are used for heavy applications with pulley mechanisms.



Figure 2. 3. Left: overhead crane with one girder and rope hoist stores material in a mezzanine. Right: Jib crane with chain hoist and motorised column (source: Pelloby Cranes)

Storage with cranes can be useful in case of storage on the floor with large horizontal spaces without the need to occupy vertical space. Another way to optimize space is to have a mezzanine floor with free vertical access for the crane. The loading and unloading surface and the storage surface are therefore at different heights. In this way, crane storage can be competitive with other automatic systems.

2.2. Inertial measurements

An in-depth analysis of inertial measurement systems is important to fully understand what opportunities there are by implementing these sensors in the control of mechanical systems and above all, checking their limits.

This chapter is based on work (Wen 2019).

An inertial measurement unit (IMU) is a sensor that integrates accelerometers for three axes (x , y , z) to detect linear acceleration and gyroscopes to detect rotation rate along three axes (yaw, pitch, roll).

The IMU can be integrated on the object under measurement in two ways:

- stable-platform design; the accelerometers and gyroscopes are mounted in a platform inside a motor-controlled gimbal structure. The relative angles between the platform and the frame can be measured at the bearings of the gimbals to directly determine the angle of rotations of the object. A well-designed structure provides great accuracy and robustness, and linear position and rotation are independent of each other. it is widely used in aerospace applications. The drawbacks are high costs and considerable weight and volume.

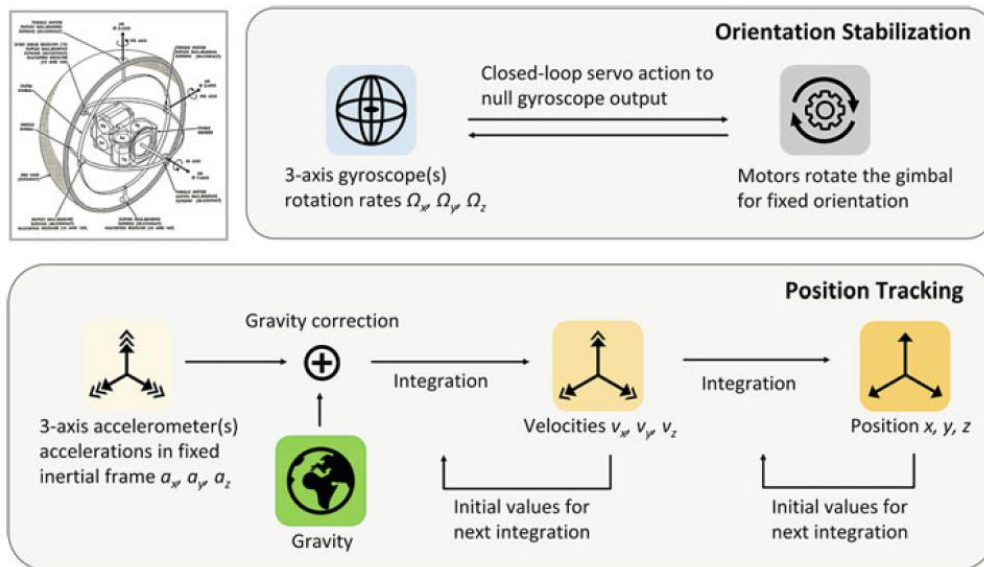


Figure 2. 4: scheme of stable-platform IMU operations (Wen 2019)

- Strapdown design; the instruments are rigidly fixed on the object. they are more suitable for small and low-cost applications. To obtain absolute rotation and position, we need to integrate respectively the angular velocity from gyroscopes and double integrate the linear acceleration values. A significant drawback is that the position tracking is tightly related to the orientation tracking, as elucidated in figure 2.2. The rotation angles of a strapdown system need to be evaluated constantly by integrating the gyroscope output. As a result, strapdown systems are vulnerable to gyroscope error accumulation and propagation.

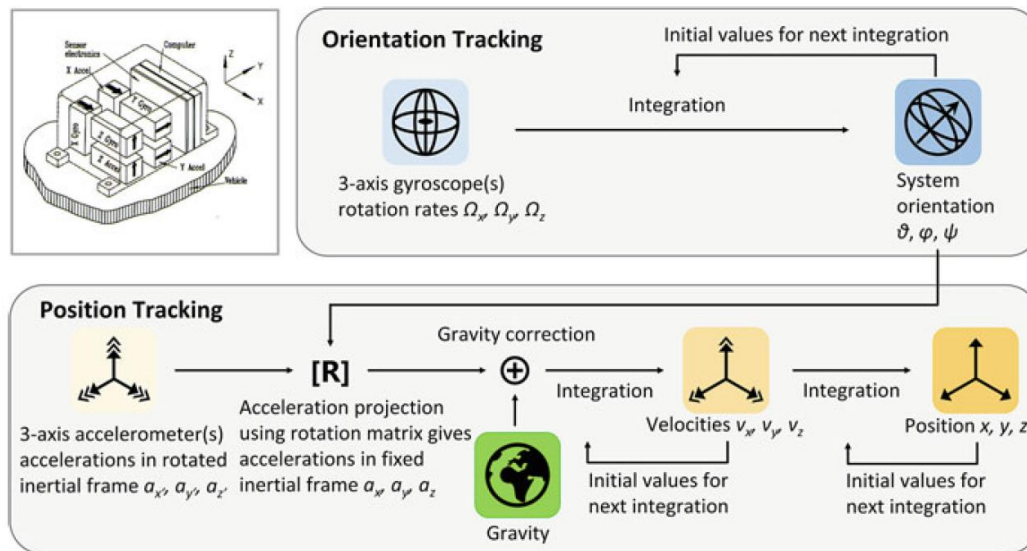


Figure 2. 5: scheme of strapdown IMU operations (Wen 2019)

2.2.1. MEMS gyroscopes

We can exploit various physical phenomena to detect inertial rotations:

- Classical mechanical gyroscopes based on conservation of angular momentum;
- Laser and optical gyroscopes based on phase shift of light beams;
- mechanical gyroscopes based on vibration induced by Coriolis force;

The last phenomenon is the most suitable for small and low-cost applications.

The gyroscope consists of a spring-mass element that oscillates along the primary direction (drive mode) in a resonant mode by an external alternating force. Orthogonal to the primary direction, the element vibrates in a secondary direction (sense mode) under the effect of Coriolis force.

The explanation of Coriolis force is based on the following equation:

$$F_{coriolis} = -2 m \Omega \times v$$

Where m is the mass of the element, v is the velocity of vibrating element and Ω is the rotation rate to be measured.

The cross product between the velocity vectors causes the force to be orthogonal to the primary direction. The vibration in this direction is detected by capacitive electrodes with nanoscale gaps. The simple model explains better these concepts.

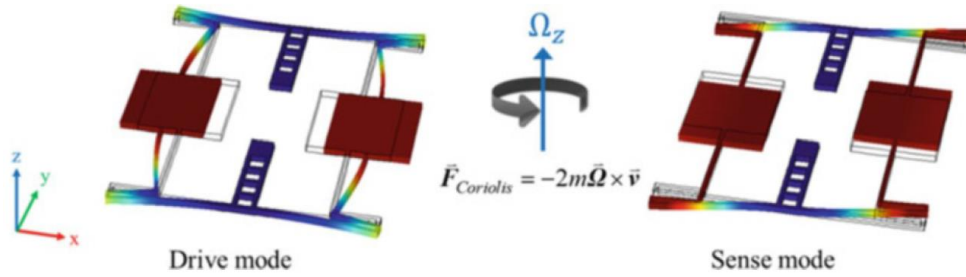


Figure 2. 6: operational mode shapes for yaw detection (Wen 2019)

There are two different designs for gyroscopes operating in yaw and pitch or roll direction, in order to place them in the same plane. Optimal structure designs that are resistant to linear vibration and thermal deformation are shown in figure 2.7.

The 3-axis gyroscopes are implemented using one quasi-solid disk yaw gyroscope and two framed-annulus gyroscopes orientated in orthogonal directions.

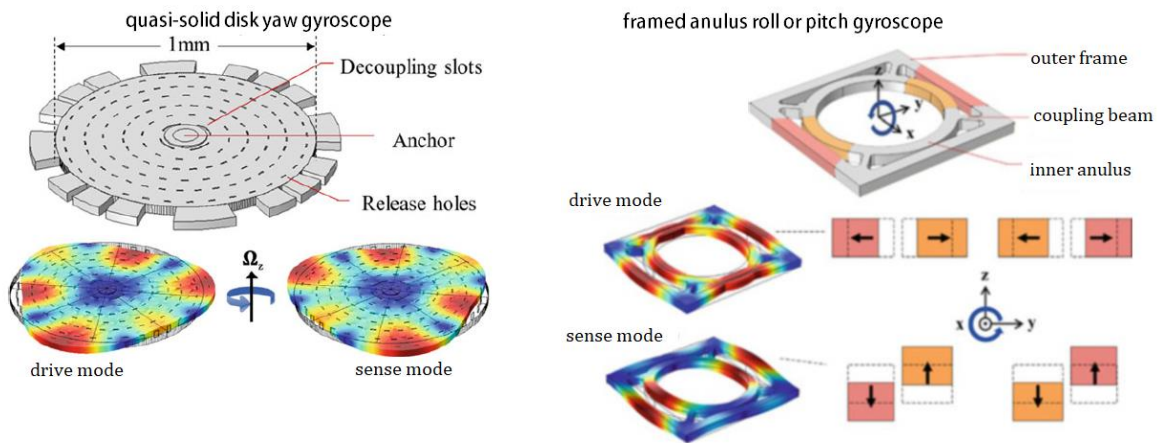


Figure 2. 7: optimised designs for MEMS gyroscopes (Wen 2019)

As said before, the rotation is computed integrating the signal from the gyroscope. This signal is subject to various errors. They are caused by changes in structural parameters (stiffness, damping), quadrature error (drive mode not perfectly orthogonal to sense mode), temperature gradient, noise in the electronic components. We can distinguish two types of errors:

- angle random walk; it is due to random white noise in the system, and when it is integrated over time, results in a zero-mean angle error with a standard deviation proportional to the square root of integration time; it is measured with a unit of $[\text{°}/\sqrt{\text{s}}]$.
- Long term drift; There are two types of long term drift: flicker noise, that shows a flat bias variation floor; The second type is a deterministic drift due to the

environment effects which increases over time with a rate random walk or a rate ramp. A regular and effective calibration is needed to avoid significant errors.

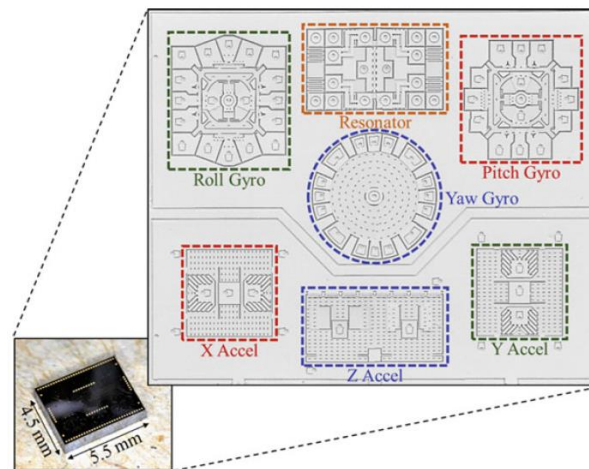


Figure 2. 8: integrated IMU with gyroscopes and accelerometers (Wen 2019)

2.2.2. Sensor fusion and Kalman filters

Sensor fusion is a term that indicates a series of methods to obtain more information on the measured variables respect to analyse sensors individually.

The advantages of sensor fusion are (Elmenreich 2002):

- Improving robustness and reliability;
- Extending spatial and time coverage;
- increasing accuracy and resolution;
- reducing ambiguity and uncertainty;

One of these methods regard Kalman Filtering. This is an algorithm that provides estimates of unknown variables from measurements given by a multitude of sensors. Optimal results are obtained when the Kalman filter is applied to linear models with Gaussian noises. Kalman filters have relatively simple form and require small computational power and small memory (Youngjoo and Hyochoong 2018). For these reasons, they are suitable for real-time applications.

Each instrument has numerous error sources. For example, a gyroscope bias makes the device appear to be spinning, a magnetometer suffers from heading errors, and so on. A powerful application of sensor fusion can be found in navigation systems. Autonomous vehicles, aircrafts, satellites, drones, use a large variety of sensors to achieve the best results. Common sensors used in navigation are global positioning system (GPS), accelerometers, gyroscopes, magnetometers, Cameras, Proximity sensors, barometers, radar (Gajjar 2017).

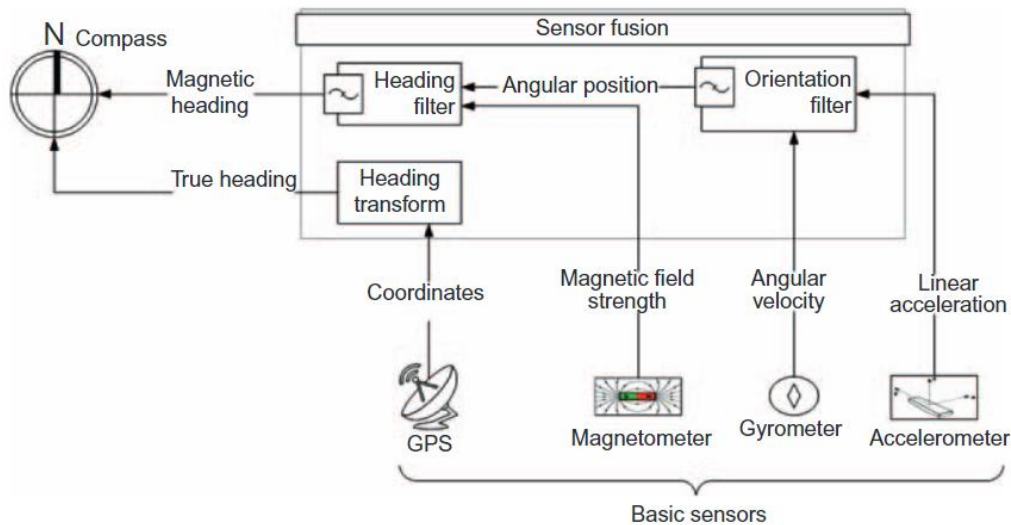


Figure 2. 9: Sensor Fusion scheme integrating inertial navigation system and GPS to detect orientation (Gajjar 2017)

2.3. Simulation environment

There are many simulation environments for multibody dynamics and control logic.

The difference between these programs lies in the complexity of the simulation which includes collision dynamics, integrated structural analysis (such as calculation of deformations of flexible components or evaluation of mechanical stress), methods of numerical solution of equations, but also the availability of integrated tools and ease of use.

MSC Adams represents one of the most used tools. This tool allows to effectively calculate the mechanical stress, deformations, contact forces of complex components during dynamic simulation. It also allows you to simulate the behaviour of actuators and sensors, managed by a control system.

Other softwares are instead strongly oriented on the programming side of mechanical systems control logic. Webots is specifically designed for robot simulation. It allows a simplified approach of the system from the point of view of control logic, allowing to write the code in different languages such as C, C ++, Java, python. Many tools are available for intelligent control, such as genetic algorithms, or for processing images from a virtual camera. the simulation takes place in real time.

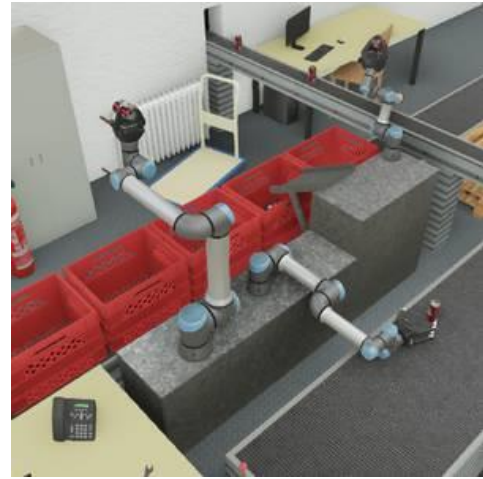
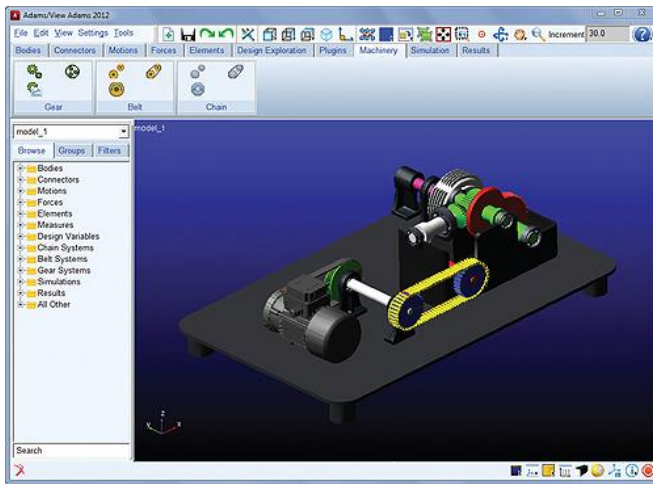


Figure 2. 10. Left: MSC Adams software for mechanism simulation. This software is widely used for automotive and aerospace engineering, consumer products, machinery (Web source: MSCsoftware.com). Right: simulation of robotic arms in a line production in Webots. This software is used for simulation of wheeled robots, industrial robots, flying drones, autonomous guided vehicles (Web source: Cyberbotics.com)

Since structural analysis is not in the interest of the thesis, the MSC Adams software has been excluded. However, it remains a useful tool for a hypothetical development of future prototypes of LHD.

For Webots software, there was some problem of accuracy and repeatability of the results during operation, perhaps due to errors of numerical integration of the physics engine. At the end, a compromise between the need for precision of calculation and ease of writing of the control logic is represented by Matlab.

The simulation of the model has been implemented using two Matlab toolboxes: Simscape Multibody and Stateflow.

The reason for the choice lies in the simplicity of use, the vast documentation available, the possibility of integrating systems with different degrees of complexity, the possibility of using built-in toolboxes for control and curve fitting.

The drawbacks are the impossibility to simulate flexible components (such as the cables) and complex meshes for simulating contact forces are quite difficult to implement.

A partial description of Simulink toolboxes potentiality is exposed in the following paragraphs.

2.3.1. Simscape Multibody

Simscape Multibody provides a multibody simulation environment for 3D mechanical systems. It is possible to model multibody systems using blocks representing bodies, joints, constraints, force elements, and sensors. Simscape Multibody formulates and solves the equations of motion for the complete mechanical system. It is possible to

import complete CAD assemblies, including all masses, inertias, joints, constraints, and 3D geometry, into the model.

Main blocks used for the simulation are:

- Joint blocks: they provide degrees of freedom to the system; the motion of the joint can be evaluated as free joint, and the torque is computed from stiffness and damping coefficient (when present); otherwise, the motion is provided by an external input, usually the motor behaviour; the torque is computed to ensure the motion, and gives information about required motor performance.
- Belt cable blocks: they model cables behaviour used by the hoist. The cord is always taut and the behaviour is ideal: inextensible and massless. Its effective length can change only if a source of a cord is provided, for example, putting a spool. This distance is monitored during simulation, through calculations based on the placement and geometry of the pulleys. The Pulley block represents a grooved or toothed wheel wrapped in a cord. The pulley is frictionless, with zero slip permitted between its surface and the surrounding cord. The cord can enter and exit at a certain angle to its centre plane. This angle can vary during simulation.
- Transform blocks: rigid transforms rotate and translate the follower frame. The frames remain fixed with respect to each other during simulation.
- Spatial contact force blocks: The Spatial Contact Force block models the contact between a pair of bodies using the penalty method. This method allows the bodies to penetrate a small amount to compute the contact forces. The block applies normal and frictional contact forces between the two bodies.

2.3.2. Stateflow

Stateflow provides a graphical language that includes state transition diagrams, flow charts, state transition tables, and truth tables. Stateflow enables you to design and develop supervisory control, task scheduling, fault management, communication protocols, user interfaces, and hybrid systems.

Control systems design relies heavily on state machines to manage complex logic. Within the thesis, a flowchart based on finite state machines is used to manage and illustrate simple operations such as picking up, transporting and stacking a box. Finite state machines are representations of dynamic systems that transition from one mode of operation (state) to another. The flowchart shows how an operation of this type is feasible with the dynamics implemented and the sensors used. It is important to measure the timing of operations and analyse safety issues.

3 Prototypes description

3.1. First design

The basic structure of the model consists of ITEM profiles (modular construction profiles for fast prototyping), which are screwed into a small load carrier. The 40mmx40mm thick aluminium profiles allow height adjustment of the carrier plate on which the electronic components are mounted. Ropes are attached to the corners of the frame and connect the model to the swivel hook. The ropes run together in a pyramid shape. ropes are made of aramid fibres, which have a higher tensile strength than steel. It is driven by a brushed dc motor. the IMU and the camera are built into the bottom of the frame. The device is used as a test bench to test any critical issues in the theoretical operation (Seifert 2019).

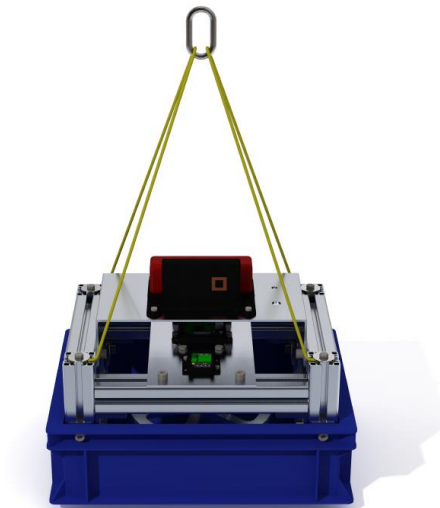


figure 3. 1: CAD model of first design (Seifert 2019)

The goal of the tests:

- Verify whether the PID controller correctly work.
- Verify whether the camera correctly detects the angle.
- Evaluate the IMU drift; the IMU is not able to recalibrate itself because the magnetometer is turned off, because it is affected by the magnetic field of the motor.
- Recalibrate the IMU; instead of the magnetometer, the IMU is recalibrated by using the relative position obtained from camera; Kalman filters are used to reduce errors in measurement data so that they are compensated for by estimates. Since

time performance is essential, a simplified version of Kalman filter, called RTQF, from the RTIMULib library is used. The RTQF filter is a modified version of the Kalman filter, which does not use matrix inversions and therefore has better performance than the Kalman filter.

The testbench is set up in the following way: the device is hanging on the hook linked to the bridge crane with a chain; during the tests, the hook is rotated with the device in order to minimize the influence of chain stiffness and friction on the hook. Below the device, there is an A4 sheet with two black circles printed on it. From images taken by the camera, the controller is able to calculate the orientation of two circles. This value represents the error to be reduced as much as possible.

Three series of tests have been conducted; the first series are intended to test the PID controller. The controller gives an input of 90° and reads the feedback signal from the IMU. The camera is disabled.

The second series is intended to compute IMU drift.

The third series shows how the Kalman filter acts with camera and IMU signals.

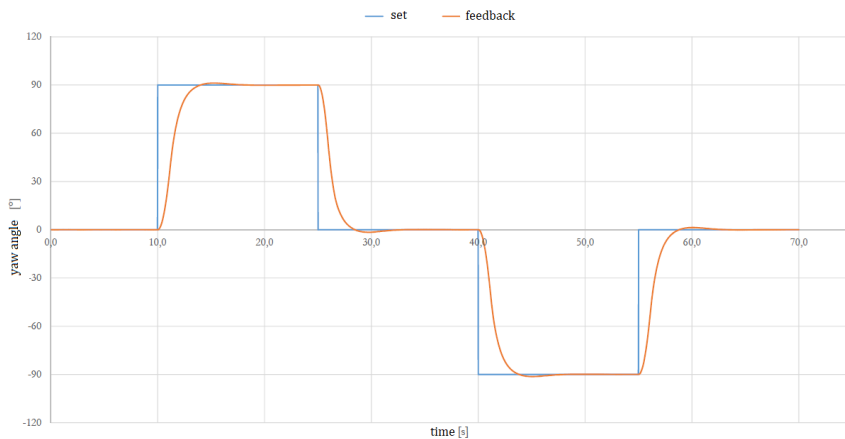


figure 3. 2: results for PID control without recalibration of IMU

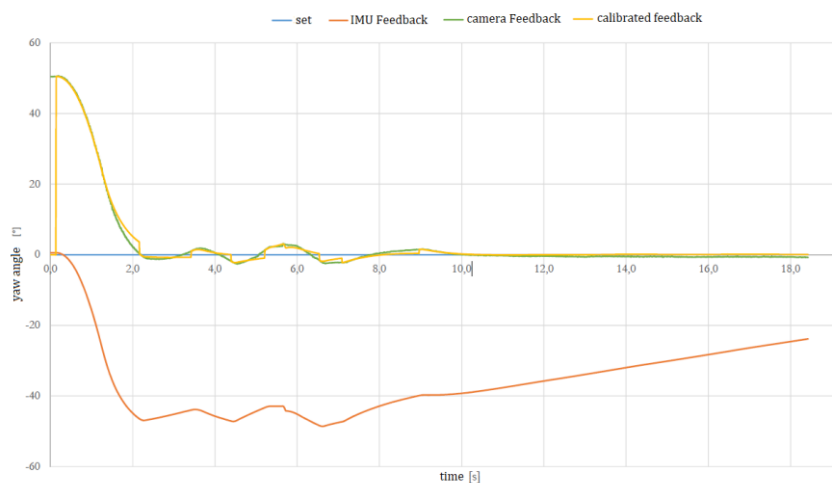


figure 3. 3: results of recalibration of IMU with camera data

IMU sample frequency	50 Hz	Frame inertia (from CAD)	175,6 g mm ²
Camera sample frequency	42 Hz	RW inertia	2,06 g mm ²
Camera resolution	256x256 pixel		

Table 3. 1: parameters for first design experiments

3.2. Second design

Fischer built a complete device based on RW principle. Besides, novel concepts have been introduced:

- A counterweight is positioned in the middle of the device. Its function is to guarantee the parallelism with the floor in presence of unbalanced loads;
- An operating gripping mechanism allows the closure and release of the box;
- A brushless dc motor is used instead of a brushed motor;
- The device uses a new IMU component (IMU brick 2.0). the magnetometer has an increased resistance to external noising magnetic fields.

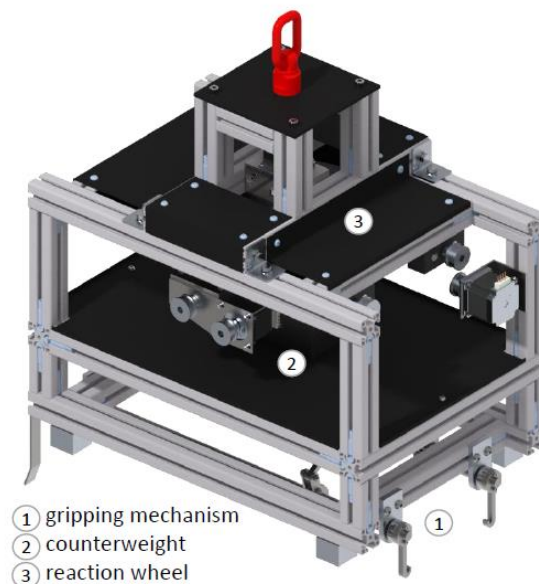


figure 3. 4: CAD model of second design (Fischer 2019)

Since the prototype is part of the experimental tests conducted in this thesis, a more detailed description is required. The device can be described starting from sub-components.

3.2.1. Actuation system

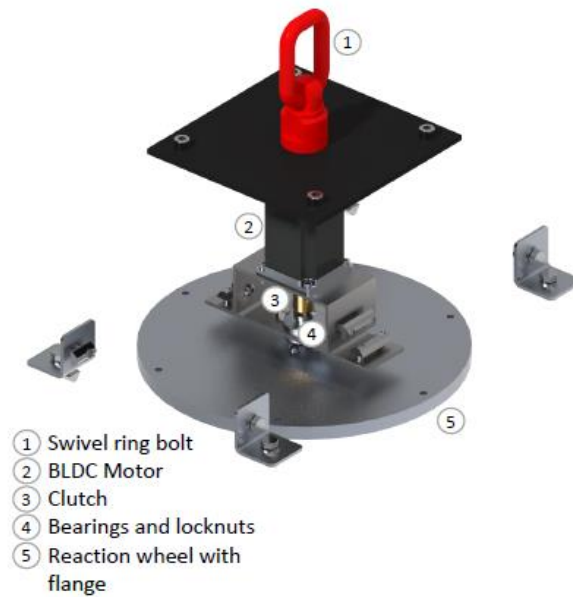


figure 3. 5: CAD model of the actuation system (Fischer 2019)

The system is composed of:

- the reaction wheel;

Radius	125 mm	Density (aluminium alloy)	2700 g/cm ³
Thickness	12 mm	Inertia	0.0175 kg·m ²

- brushless DC motor (model 57BLF03) coupled with motor driver (BLDC-8015A);

Number of poles	8	Rated voltage	24 V
Number of phases	3	Rated speed	3000 rpm
Max speed	8000 rpm	Output power	188 W
Rated torque	0,6 N·m	Rated current	12 A
Peak torque	1,8 N·m	Peak current	36 A
Torque constant	0,066 N·m/A	Rotor inertia	220 g·cm ²
Back electromotive force	6,3 V/krpm	Body mass	1,24 kg

- wire-wound resistor (model HS150 3R3 J); It is used to dissipate heat generated by the motor braking;

Resistance	3,3 Ohm	Rated power	150 W
------------	---------	-------------	-------

- lithium-polymer battery as source power for the motor;

Rated voltage	22,2 V	Capacity	4600 mAh
---------------	--------	----------	----------

3.2.2. Balancing system

The device balance is entrusted to a mobile mass, that is a brick of steel with dimensions 180x120x60 mm and mass 10 kg.

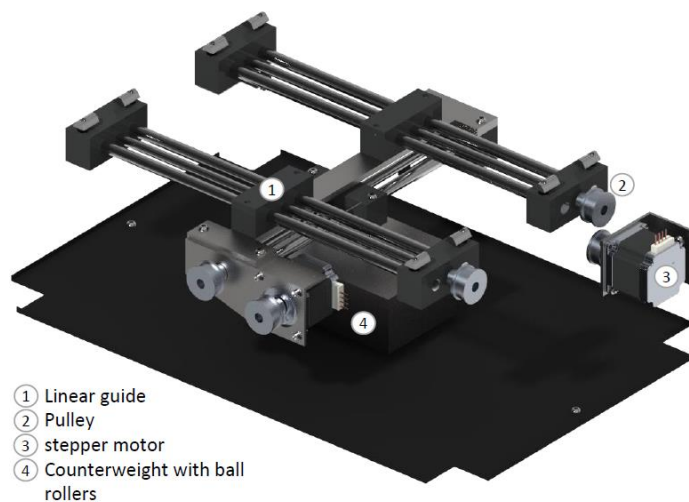


figure 3. 6: CAD model of the balancing system (Fischer 2019)

3.2.3. Gripper mechanism

Two couples of hooks allow the device to grip the box.

Each couple of hooks is fixed on a shaft. A small linear actuator rotates the shafts through the levers. The stroke of the actuator is 15 mm. two limit switches detect the reaching of the upper and lower position.

The hooks are meant to enter into the elongated holes present in the upper side of the box. When the device stays in the predefined position, the actuator is activated and reaches the lower position. In this way, the hooks grip the box when the device moves upwards.

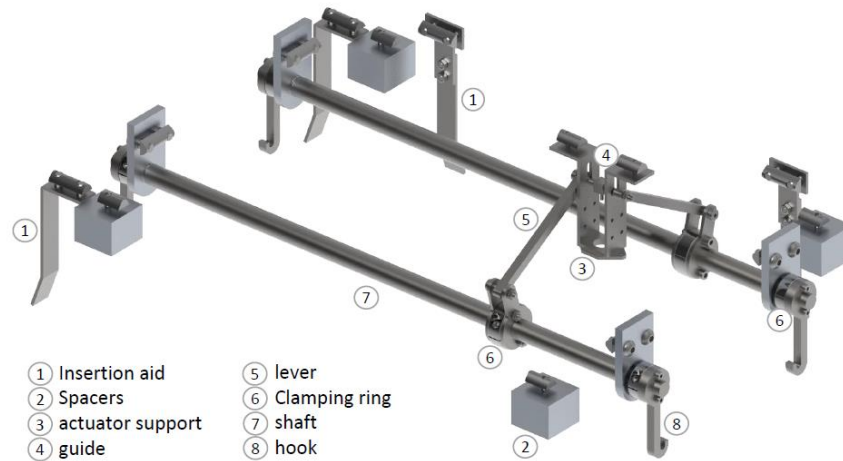


figure 3. 7: CAD model of the gripping system (Fischer 2019)

3.2.4. Sensor system

The device has two main sensors:

- An inertial measurement unit (IMU Brick 2.0). This component integrates three-axis accelerometer, magnetometer and gyroscope and provides the angle position, angular velocity, linear acceleration, gravity vector in reference to an inertial coordinate system. The table resumes the characteristics of the sensor.

Acceleration, Magnetic, Angular Velocity Resolution	14 bit, 16 bit, 16 bit
Heading, Roll, Pitch Resolution	0.0625° steps
Sampling Rate	100 Hz

- The camera is positioned on the underside. The controller uses YOLO object detector as algorithm to measure position and rotation of the object. The sampling frequency of such system is relatively low, that is 1 Hz (Herz 2020).

3.2.5. Control system

Successive works have implemented the camera operation and the control system on the prototype (Herz 2020). The input variable is the duty cycle of PWM and it is proportional to the angle error.

4 Experimental tests

4.1. Mathematical model

In this paragraph the linear equations of motion of the LHD around its vertical axis are described. It is supposed that the actuator moving the reaction wheel can be described as a DC motor.

The equation of a DC motor is:

$$V = Ri + k\omega$$

Where V is the voltage source, i is the current, R is the resistance of the wires, k is the speed constant of the motor, ω is the relative angular velocity of the reaction wheel relative to the frame, the product $k\omega$ is the back-electromotive force.

The second equation connects the motor torque T_m to the reaction wheel velocity. c_p is the linear constant of the friction in the joint between the wheel and the frame.

$$J\dot{\omega} + c_p\omega = T_m = ki$$

The third equation links the absolute angular position of the frame with the reaction torque of the inertia momentum.

$$I\ddot{\theta} + c_t\dot{\theta} = J\dot{\omega}$$

Where c_t is the linear constant of the friction in the joint between in the swivel hook.

Laplace transform is applied to change the differential equations in time domain in algebraic equations in frequency domain, where s is the Laplace variable.

$$i = \frac{V - k\omega}{R}$$

$$\omega = \frac{k}{Js + c_p} \cdot i$$

$$\theta = \frac{J}{Is + c_t} \cdot \omega$$

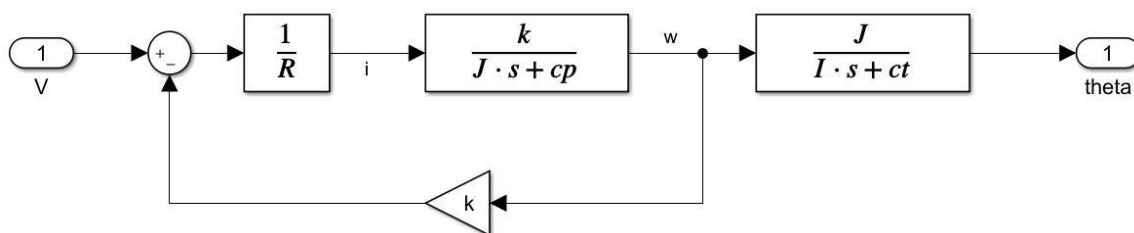


Figure 4. 1: Simulink block diagram of the open-loop response with motor voltage as input and angular position of LHD as output

4.2. Test description

To estimate properly the parameters and friction function, we need new and accurate measurements. angular speed measurements from the yaw gyroscope are appropriate for the purpose and sufficiently reliable, since these measures are directly sensed (no integration or derivation is needed) and frequency sampling is high.

The output data are:

- Rotation of the LHD from IMU θ ;
- angular speed of the LHD from IMU $\dot{\theta}$;
- angular speed of the RW from Hall effect sensors ω ;

The input data is the duty cycle and represents the fraction of the maximum signal value given by the Raspberry Pi board to the motor driver with a frequency of 50 Hz; a duty cycle of 100% corresponds to the motor speed equal to 3000 rpm.

During the tests we can observe that the device is free to rotate around its vertical axis thanks to the swivel hook. A chain links the ring bolt to the crane hook.

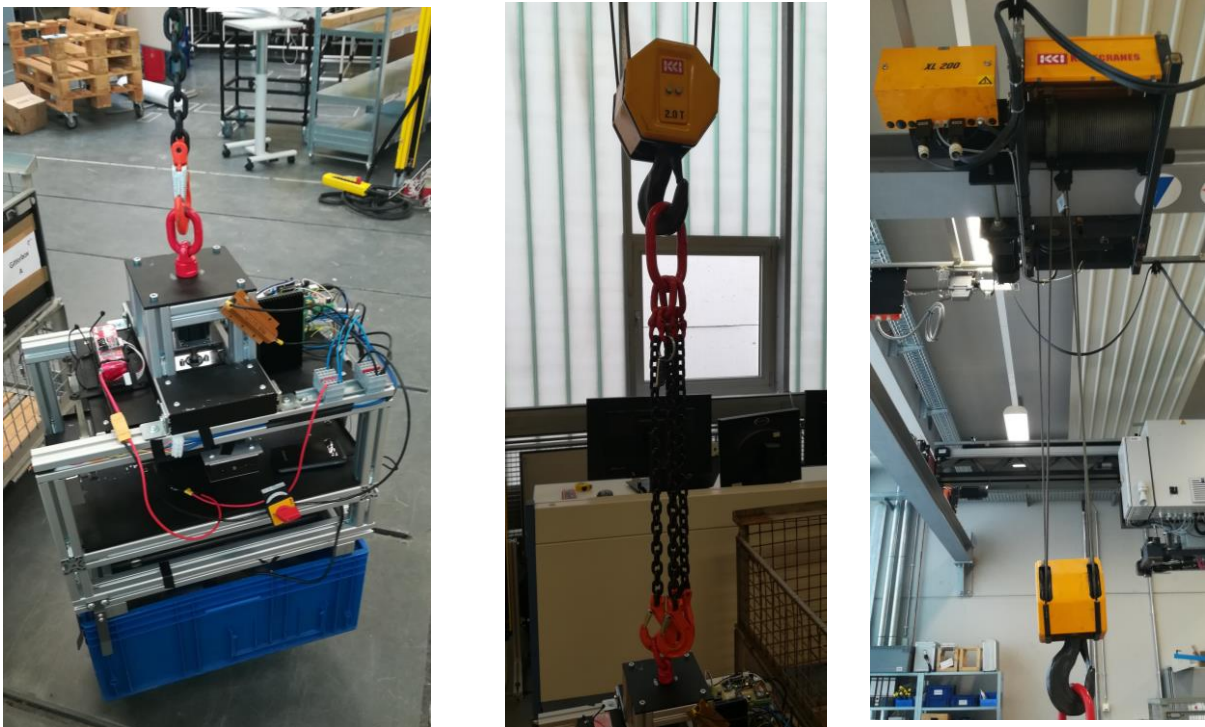


Figure 4.2. Left: prototype of LHD with LKT used for the tests. It is suspended from the ground by about 10 cm. Centre: the chain linking the LHD to the crane hook. Right: the hook and the trolley of the overhead crane in IFL.

The parameters to be estimated for the implementation of the virtual model are:

- inertia of LHD around its rotation axis;
- Transfer function of BLDC motor;
- Torque motor saturation;
- function of the friction force in the swivel hook;

4.3. Test results

Two types of tests have been conducted: The first series of tests consists of an open loop response with different step inputs of duty cycle (100, 75, 50 and 25%). The duty cycle is set to the step value and then, when the device is stopped for a sufficiently long time, the duty cycle is set to zero and the motor decelerates the reaction wheel. Several trials have been conducted for each step of duty cycle (figure 4.1).

They are useful to take a first look at the output trend. From Hall sensor data, we can observe that motor response is quite slow: it takes about 9 seconds to reach full speed and 6 seconds for half the speed. The breaking torque is lower when the speed is under 900 rpm.

Comparing $\dot{\theta}$ and ω curves, it is noticed that when the RW is accelerating, $\dot{\theta}$ and ω have the same trend.

Besides, it has been noted that the return force of the link chain towards its rest position is not negligible. We can observe that when the device stops, there is a little displacement in the opposite direction due to this chain behaviour.

The second series of tests examines the linear response. These results allow a better understanding of the motor dynamic response and chain behaviour. The results are more dispersive than the previous ones. Two examples of tests with a slope of 2 and 3 %/s are shown in (figure 4.2). In total, tests with slope 1, 2, 3, 4, 8 %/dc have been conducted.

Besides, some tests have been conducted by blocking the rotation of the swivel hook, to obtain information about chain's behaviour. All these experiments will be shown in the following chapter comparing with the simulation, with the intent not to duplicate all the results and overloading the treatment.

Experimental tests

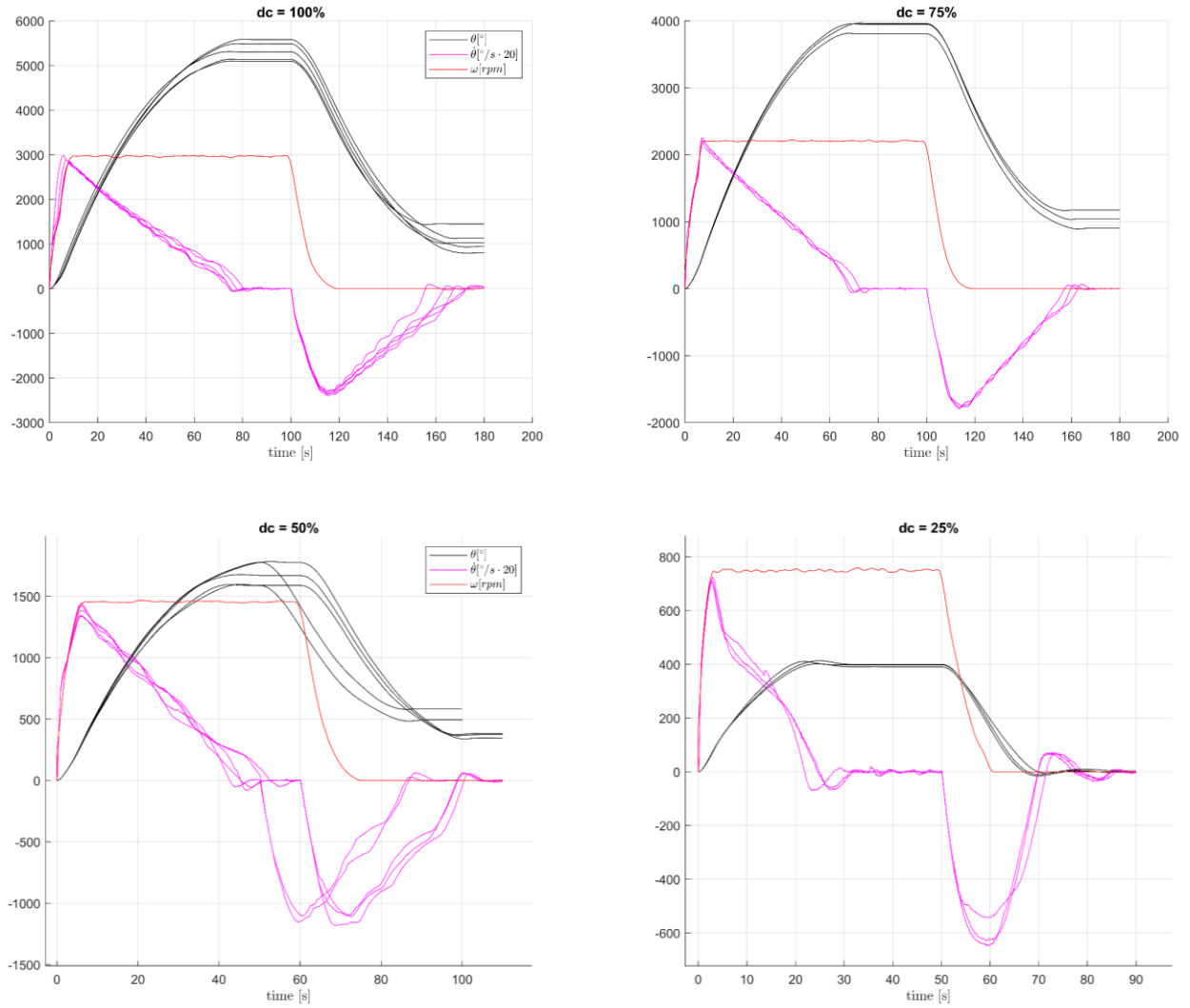


Figure 4. 3: Step response with duty cycles of 100%, 75%, 50%, 25% of the maximum motor speed

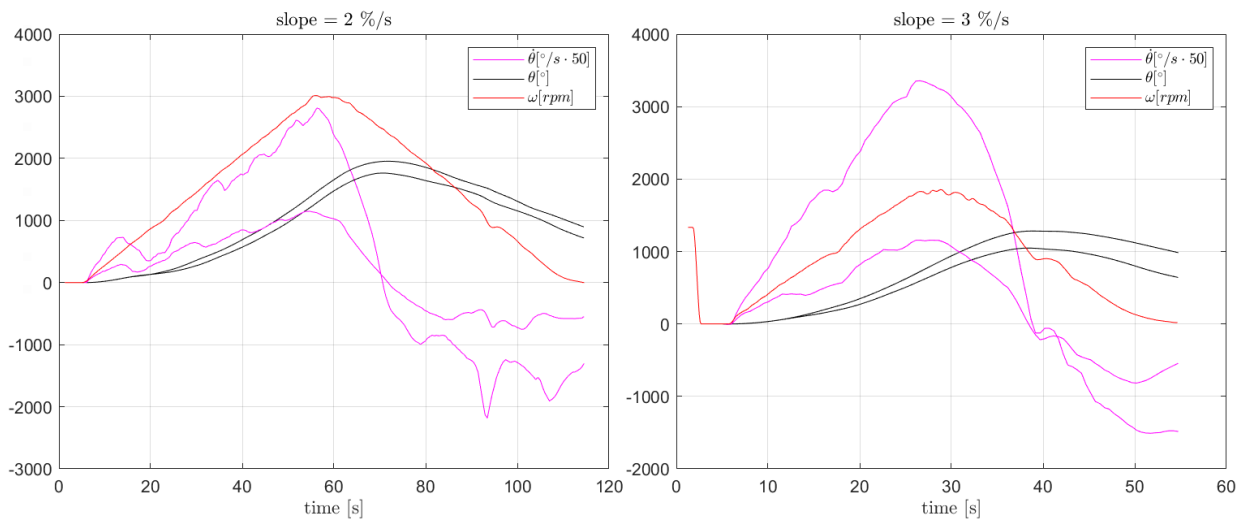


Figure 4. 4: linear response with an increment of 2 and 3% in the duty cycle per second

5 Vertical axis motion simulation

The model of the movement of the device along the vertical axis was obtained by following four steps:

- Actuation system modelling
- Inertia and friction evaluation
- Chain behaviour modelling

5.1. Actuation system modelling

The first step of the model begins from the actuator model since it is independent of the other parameters (inertia, friction, etc) and therefore there are fewer independent parameters to be obtained.

The data from the Hall sensor have been filtered with the purpose of eliminating the noise.

The curve fitting method was adopted to obtain the transfer function. In particular, first order transfer functions were tested with different values for the time coefficient, trying to adapt the simulated speed curve on the experimental data from linear duty cycle functions and speed trend taken from the PID control (chapter 7).

It is not possible to obtain the motor torque directly, but an estimation can be obtained from the resulting acceleration.

The Simulink block scheme has been modelled as illustrated in figure 5.1.

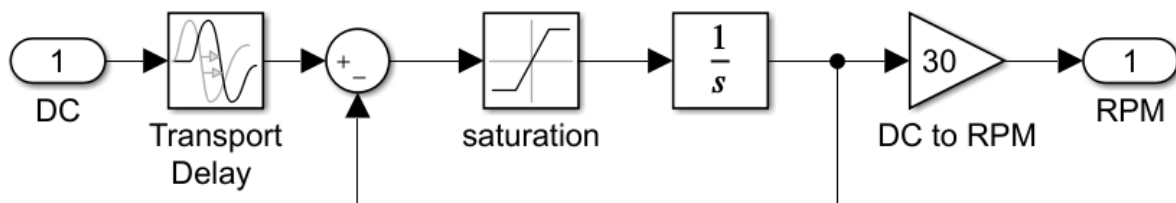


Figure 5. 1: actuator Simulink block scheme

The system includes a first order transfer function, a saturation in the acceleration, and a transport delay. The result is then converted in rpm multiplying by 30:

$$\omega = \frac{30}{\tau s + 1} DC$$

The duty cycle variation saturation is 12 %/s that corresponds to 37.7 rad/s² in terms of RW acceleration. The transport delay is set to 0.2 seconds. these values are obtained from the step response (figure 5.2). It proved difficult to figure out the reason of the actual trend. It could result from friction in the RW support and from the speed control of the motor driver.

The linear response provides the limits of use. The motor manages to get a good response up to a slope of the duty cycle set of 4 %/s. After this value the trend becomes too irregular.

At last, values were compared with data from PID control. for them, the transfer function seems to work well.

Motor parameters	value
Time coefficient τ	1
Acceleration limit	12%/s
Time delay	0.2 s

Table 5.1: motor parameters.

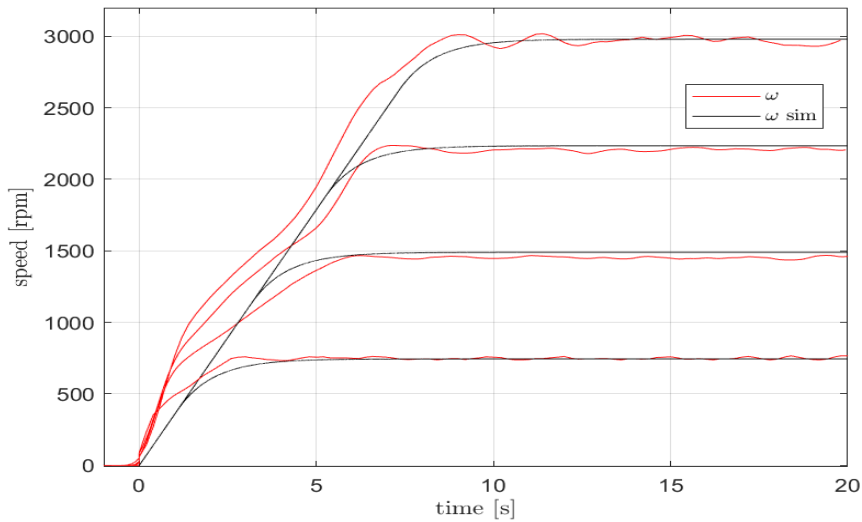


Figure 5. 2: comparison of step response of motor speed between experimental and simulated data with dc = 100%, 75%, 50%, 25%.

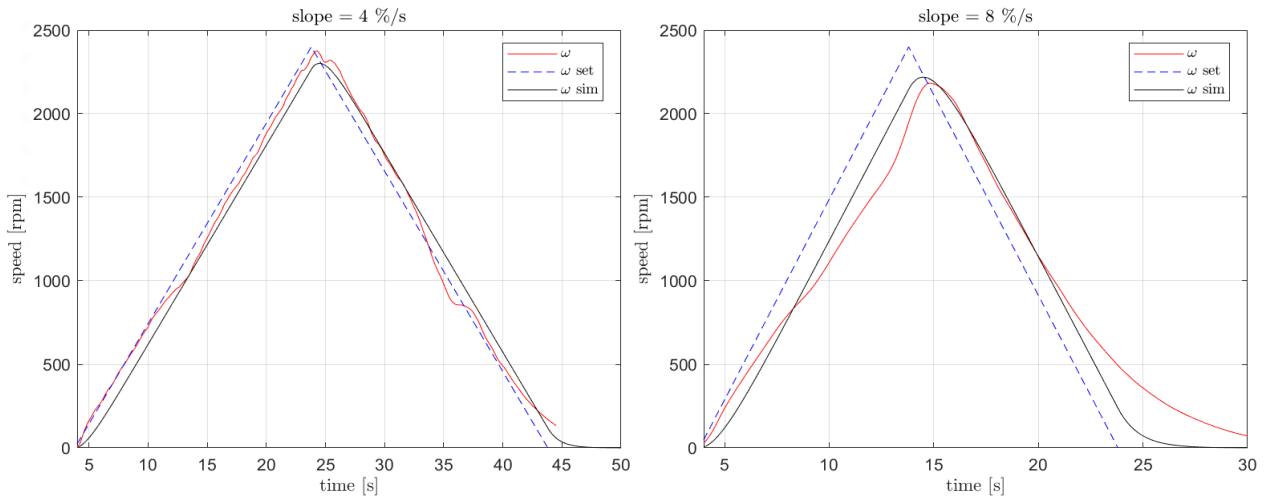


Figure 5. 3: linear response of motor speed with 4 and 8%/s duty cycle slope.

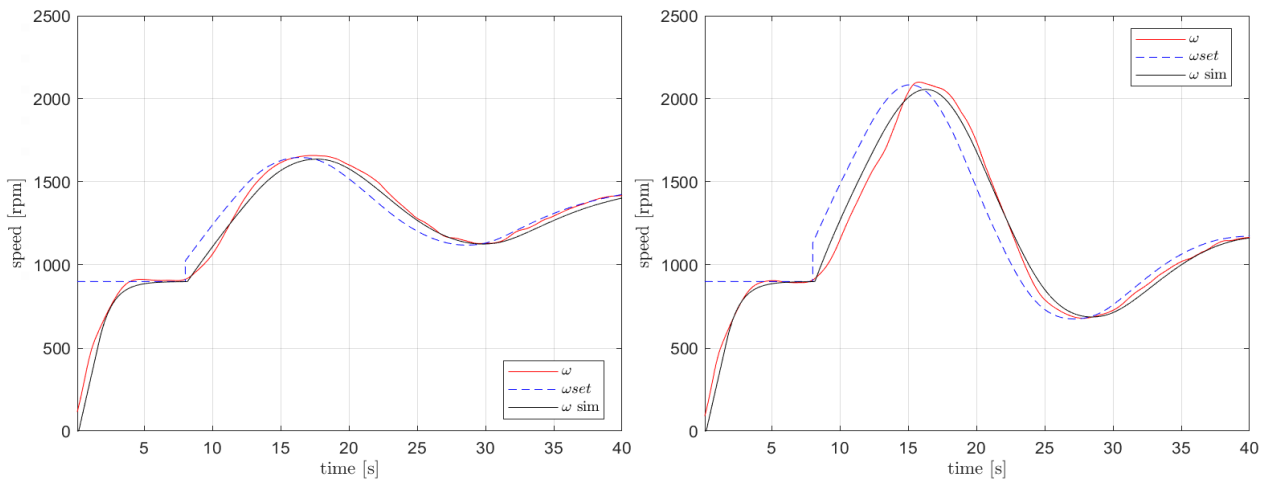


Figure 5. 4: response of motor speed during PID control. The simulated data is based on the duty cycle set of the real PID control.

5.2. Inertia and friction evaluation

Once the motor data has been obtained, it is possible to use it for the next simulations. to obtain the value of inertia and friction, it is necessary to analyse the IMU speed data from step response.

In fact, the inertia of the LHD is obtained by measuring the peak value of the speed trend, since it is directly proportional to it. the function of the friction force, on the other hand, can be obtained from the descent curve following the peak, when the motor turns at full speed. Since the slope of $\dot{\theta}$ is constant, it is deduced that the friction is mostly static. speed oscillations are due to the fact that the frictional force is dependent on the position of the hook θ . The trend is described as a trapezoidal function with a mean value of 0.065 Nm and an amplitude value of 0.045 Nm.

Vertical axis motion simulation

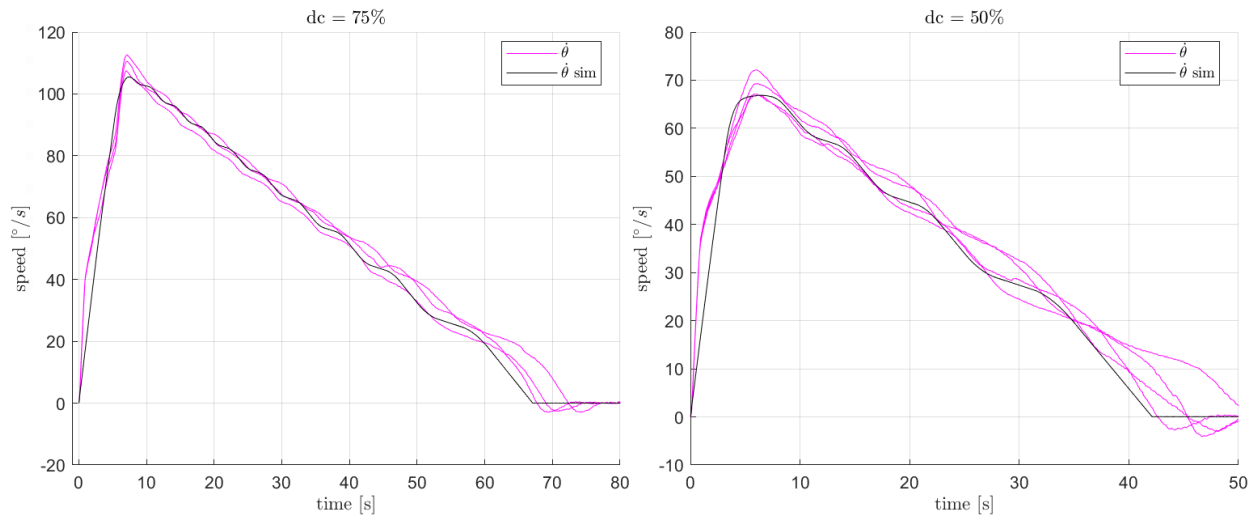


Figure 5. 5: comparison between experimental and simulated step response of 75% and 50% for inertia and friction estimation.

Table 5. 2: inertia and friction values from step response.

LHD Inertia	2 kg m ²		
Friction mean value	0.065 Nm	Friction max val.	0.11 Nm
Friction amplitude val.	0.045 Nm	Friction min val.	0.02 Nm

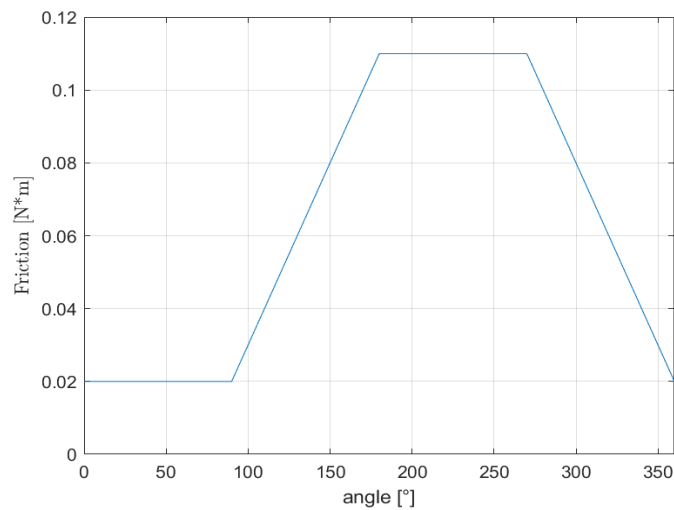


Figure 5. 6: friction function in the swivel hook used in the simulation. It depends on the position θ of the hook.

5.3. Chain behaviour

During the test, the hook is manually blocked and the device moves only thanks to the compliance of the chain. The motor runs at a constant acceleration of 1,5%/s (figure 5.7).

From the IMU data θ , it appears that the final position does not coincide with the initial position. In reality, this is due to the inaccuracy of the instrument. A visual observation of the device demonstrates that the final position is almost equal to the initial position.

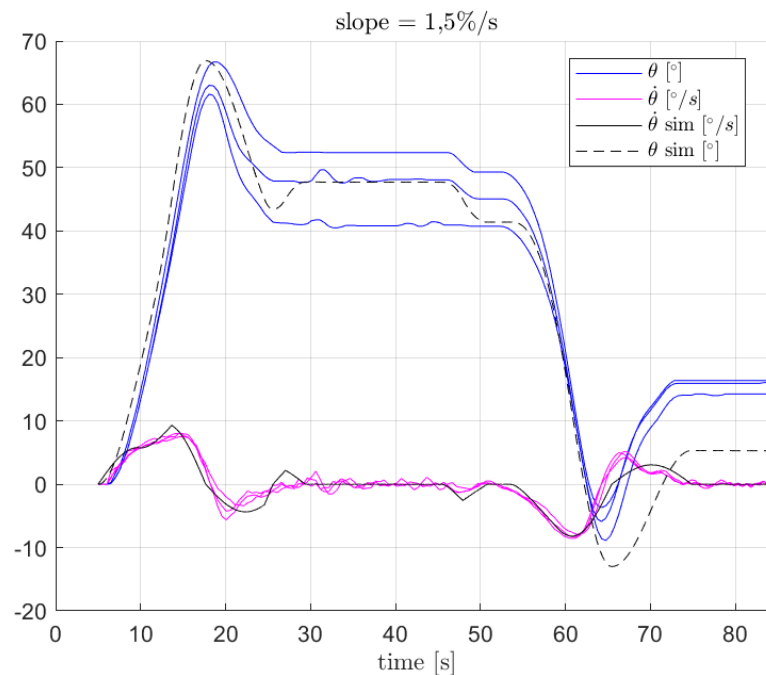


Figure 5.7: angular position and rotation of LHD when the hook is blocked.

The force that acts to the LHD caused by the chain stiffness is provided by a Matlab function:

```
function Fspring = fcn(y,y0,dyd)
ya = 10;
k = 0.39;
Fs = 0.005;
if(y-y0>ya)
    Fspring = k*(y-y0-ya)+Fs*sign(dyd);
else
    if(y-y0<-ya)
        Fspring = k*(y-y0+ya)+Fs*sign(dyd);
    else
        Fspring=Fs*sign(dyd);
    end
end
end
```

the Matlab function describes this behaviour: in the angle between -10° and $+10^\circ$ with respect to the rest position, the function output is zero. once the limit value is exceeded,

the chain gives an elastic force equal to $F = k(\theta - \theta_0 \pm 10^\circ)$, where k is the spring constant, θ is the value from IMU, θ_0 indicates the rest position of the chain relative to the hook position. θ_0 value changes when the hook rotates. A static friction is present when the LHD rotates relatively to the chain.

At last, the chain behaviour is introduced in the complete model as external force in diagram 6.1. When the motor starts, the LHD rotates twisting the chain links first. This increases the binding force of the chain, which also acts on the crane hook. As long as the chain force is less than the friction force of the hook, the LHD continues to rotate without moving the hook. once it gets higher, then the hook starts to move keeping the chain under tension. once the LHD stops, the chain releases the stored energy exerting a force in the opposite direction.

6 Control design

In the previous control scheme, the duty cycle was proportional to the angle error (Herz 2020). This chapter provides a new idea for the control design, based on the acceleration of RW as input.

6.1. Description

The equation of motion is:

$$I\ddot{\theta} = J\dot{\omega} - F(\theta, \dot{\theta})$$

Where the term $F(\theta, \dot{\theta})$ is a generic function that describes all the external forces that act on the device. $J\dot{\omega}$ is the wheel's reaction torque; control is based on the adjustment of the RW acceleration.

The main advantage of adopting this control scheme is that the integral component is able to exceed the value of external forces, if they fall within the values allowed by saturations. The proportional term now acts as a linear spring and the derivative term as a linear damper. The control function is resumed as:

$$\dot{\omega} = k_P \cdot e + k_I \cdot \int_0^t e \, dt + k_D \cdot \frac{de}{dt}$$

Where:

- dc is the duty cycle;
- e is the angle error measured by IMU;
- Δt_i is the time difference between the present and the last measurement;
- k_P, k_I, k_D are the gains of the controller.

In order to write the control program the conversion from the continuous-time model to a discrete-time model is needed:

$$\frac{\Delta\omega_i}{\Delta t_i} = k_P \cdot e_i + k_I \cdot \sum_0^i e_i \cdot \Delta t_i + k_D \frac{e_i - e_{i-1}}{\Delta t_i}$$

Where e_i and Δt_i are the error in the instant of time t_i and the interval of time between t_i and the previous instant t_{i-1} .

In the script we are able to set the duty cycle, so finally:

$$dc_i = dc_{i-1} + \left(k_P \cdot e_i + k_I \cdot \sum_0^i e_i \cdot \Delta t_i + k_D \frac{e_i - e_{i-1}}{\Delta t_i} \right) \cdot \Delta t_i$$

The integrator component needs an anti wind-up control because of the slow response due to the current limitation in the motor. The simplest method to do that is to apply a superior limit for the error summation.

In conclusion, the speed value at instant t_i is the summation of the values of PID function over time plus the initial speed of the wheel dc_0 :

$$dc_i = dc_0 + \sum_j^i PID(e_j, \Delta t_j)_j \cdot \Delta t_j$$

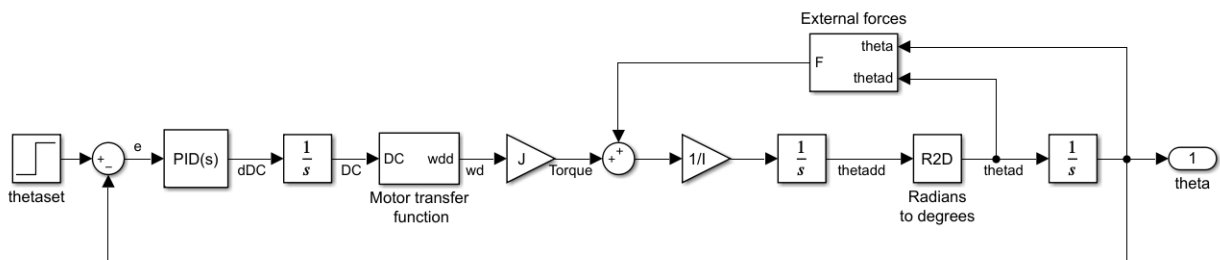


Figure 6. 1: PID control scheme.

6.2. Results

A series of experimental tests have been carried out for the purpose of calculating the best suitable parameters for the model.

The initial speed of the RW is 900 rpm, that corresponds to a duty cycle of 30%. It is necessary to overcome the inferior speed limit and the low value of brake force at low speed. The step response starts at 8 seconds.

The Matlab function correspond to the same algorithm used in the experimental tests; the function computes three components of PID control: proportional, integral, derivative. The proportional and integral components have a saturation to limit the output. The sampling period is 0,1 seconds.

```
function dcout = PID(e)
kp = 0.0035;
ki =0.0018;
kd =0.028;
Psat = 0.35;
Isat = 0.027;
dt = 0.1;
persistent esum
persistent elast
persistent dc
if isempty(esum)
    esum = 0;
end
```

```

if isempty(elast)
    elast = 0;
end
if isempty(dc)
    dc = 30;
end
P=kp*e; %proportional component
% proportional component saturation
if(P>Psat)
    P=Psat;
end
if(P<-Psat)
    P=-Psat;
end
esum=esum+e*dt;
I=ki*esum; %integral component
% integration saturation
if(I>Isat)
    I=Isat;
end
if(I<-Isat)
    I=-Isat;
end
D=kd*(e-elast)/dt; %derivative component
elast=e;
ddc=P+I+D; %deltadc
%summation
dc=dc+ddc*dt;
%speed saturation
if(dc>100)
    dc=100;
end
if(dc<0)
    dc=0;
end
dcout=dc;

```

the PID controller is tested on a series of experiments with θ set values of 90° , 135° , 180° .

Table 6.1: PID control parameters used in experimental tests and in simulated model.

Controller parameters	Without payload	With payload
kp	0.0035	0.0048
ki	0.0018	0.0018
kd	0.028	0.04
Proportional saturation	0.35	0.6
Integral saturation	0.027	0.035

The results are shown in figures 6.2 and 6.3.

The system is characterized by a high overshoot. In this way, the spring reaction of the chain is countered.

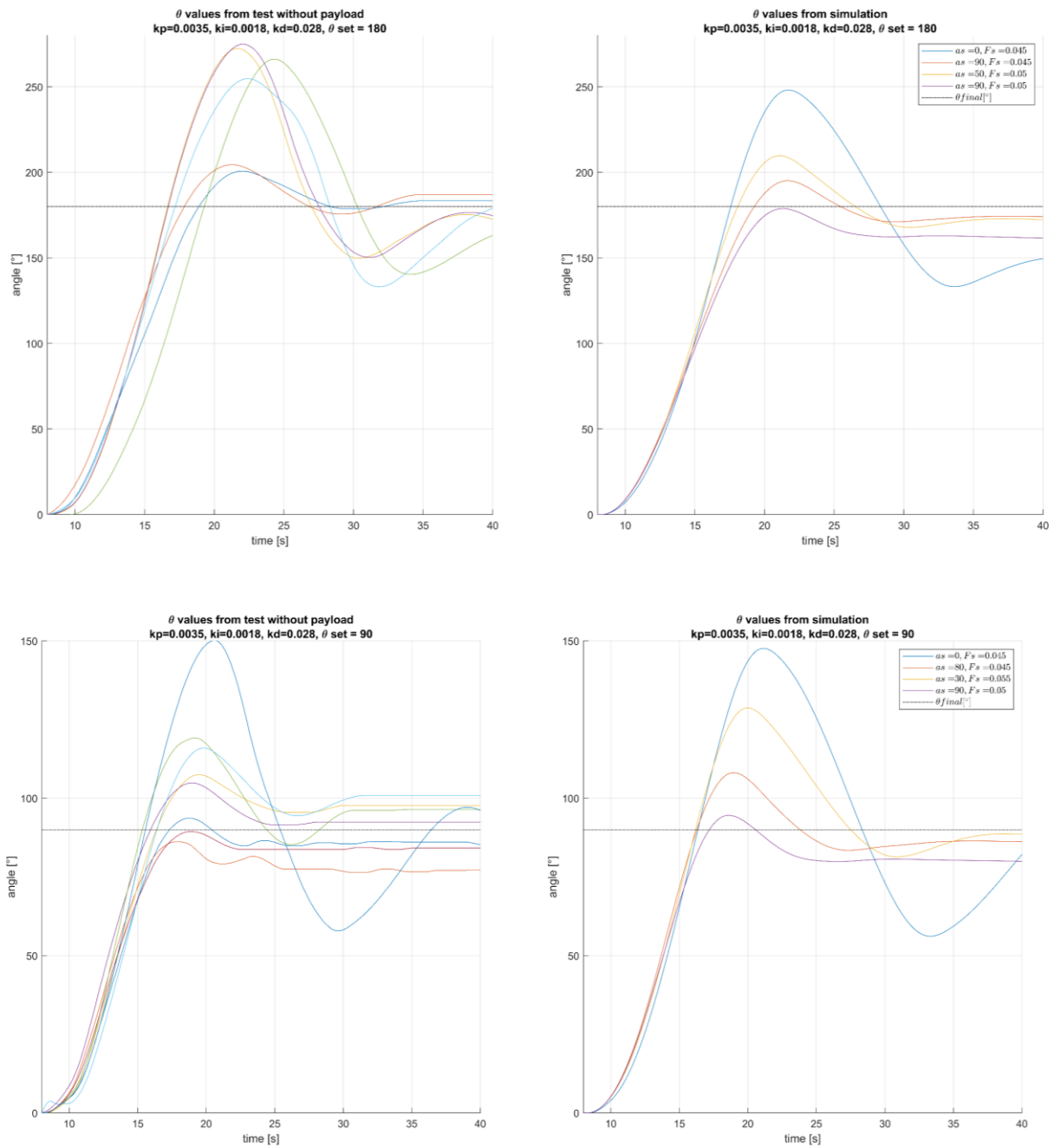


Figure 6. 2: comparison between experimental results and simulations for PID control without the payload. a_s represents the initial value of the swivel hook rotation and F_s is the mean force of friction.

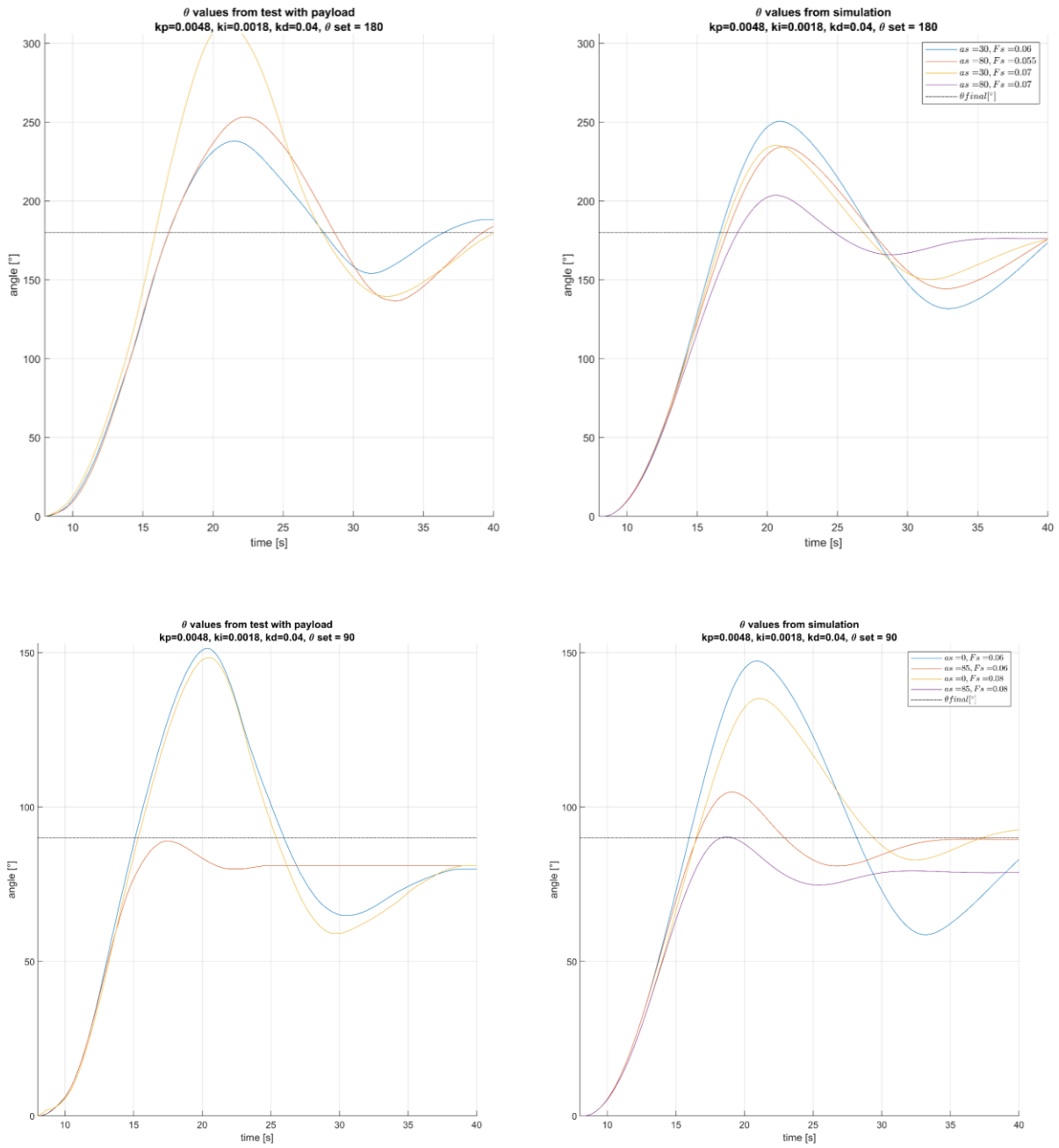


Figure 6. 3: comparison between experimental results and simulations for PID control with the payload. a_s represents the initial value of the swivel hook and F_s is the mean force of friction.

6.3. Conclusion

The results (table) are characterized by high variability. It should be noticed that the angle value is characterized by a bias of about ten degrees (visually verified by the fact that in case where the sensor indicates an almost exact value, the alignment between the device and the box is not achieved), even if this does not considerably affect the results obtained.

Table 6.2: results for PID control

	Set 90° without payload	Set 135° without payload	Set 180° without payload	Set 90° With payload	Set 135° With payload	Set 180° With payload
N° of trials	11	4	6	3	3	3
Mean	89.7	128.1	176.5	80.6	133.3	183.9
Standard dev.	7.416	13.191	8.486	0.577	4.691	4.033

In general, it can be said that the presented system fails to achieve the required precision due to the high value of non-linear forces, and it is difficult to obtain better results without structural changes.

A considerable improvement can be obtained by reducing the friction force. It can be done in two ways: eliminating as much as possible the friction of the rotating hook and eliminating the chain; the ring belt of the LHD is mounted directly on the crane hook. The other way is to insert a thrust bearing directly into the LHD so that the frame turns around this joint.

In the next chapter simulations one of these two hypotheses is considered valid. Then it is possible to simulate motion again by setting a hypothetical joint's friction force equal to 0.01Nm as the only external force (figure 6.4).

New parameters have been calculated for the control. The integrator part was set to zero, because it increased the system instability. Proportional and derivative gain are set equal to 0.13 and 0.45 respectively. The high derivative term is needed to damp oscillations of the RW around the position set. The final speed of RW is almost the same of the initial speed, due to the fact the system is conservative if the friction is negligible.

The oscillations of θ around the set value is due to the motor behaviour. It is necessary to have a smaller time coefficient to reduce oscillations.

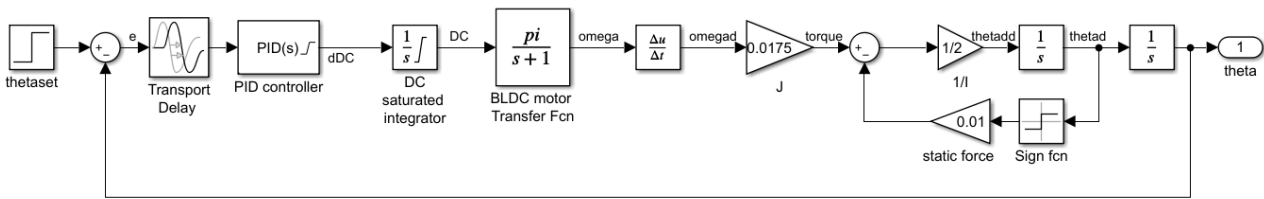


Figure 6.4: PID control used for global simulation

parameters	value
LHD Inertia	2 kg m ²
Motor acceleration saturation	8 %/s
Static friction force	0.01 Nm
Initial value of duty cycle	30%
Duty cycle saturation	0-100%
kp	0.13
kd	0.45
ki	0

Table 6.3: parameter settings used for global simulation

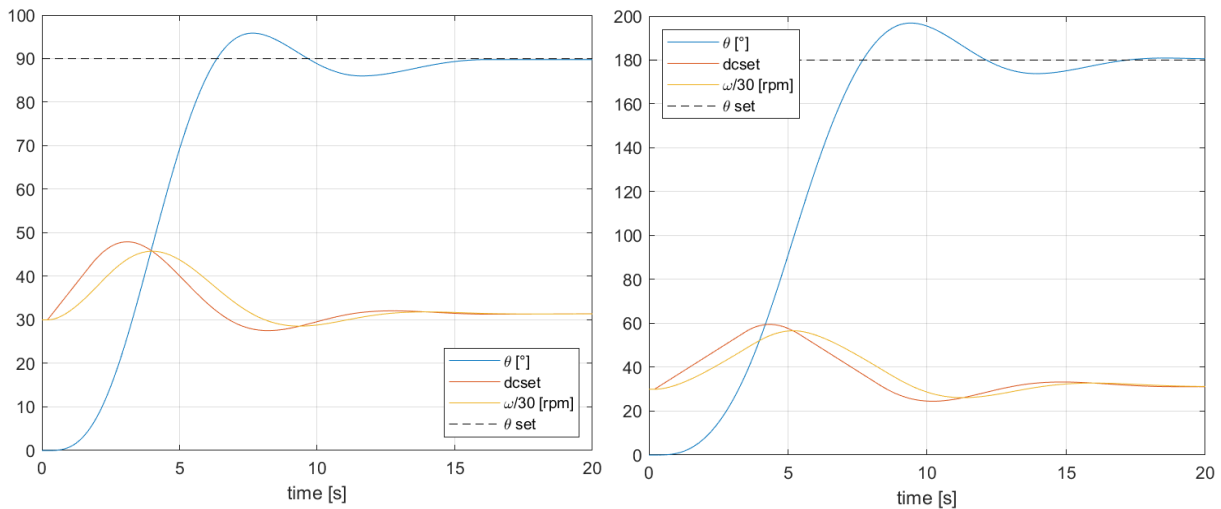


Figure 6. 5: PID control simulation with 90° and 180° step response without payload and simplified parameters for global simulation

7 KLT gripping process simulation

During this chapter, the behaviour of the LHD during the gripping process is analysed.

The overhead crane has a four ropes hoist, similar to the real model present in the IFL. the presence of 4 ropes increases lateral stiffness, but it has the disadvantage of creating small oscillations during the ascent and descent phase.

The gripping process consists of taking the KLT from anywhere on the floor and lift it off the ground. The result to be obtained is to implement a control logic that is also applicable in the real context, and to observe dynamic behaviour. The sensors are considered ideal, i.e. the position of the KLT is detected without errors.

Initially, the model used on Simscape is presented. block diagrams are not shown because they would require too much space for the exhibition. In the end the results obtained will be discussed.

7.1. Simscape model description

the model is divided into the following components:

- the crane bridge
- the load handling device
- the control logic
- the floor
- the box
- contact forces

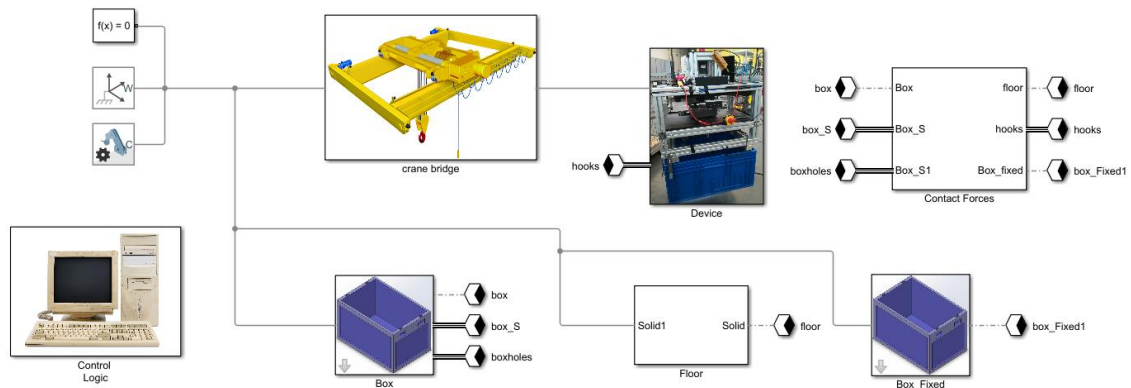


Figure 7.1: general Simscape scheme of components.

7.1.1. crane bridge

Three electric motors provide the movement of the bridge on the X axis, the trolley on the Y axis and the vertical movement of the hook in the direction of the Z axis. The type of motor used is mostly three-phase asynchronous. It is necessary to convert the electronic components to have control of the electric motors by the main controller.

If not present, position sensors must be introduced (for example absolute encoders on the motor shaft) to read the position of the 3 moving components.

Torque and speed control of the motors can be achieved in various ways: (Chan and Shi 2011):

- Pole changing: the speed and torque of the rotor is closely related to the ratio of the frequency of the electrical grid and the number of poles (called synchronous speed); increasing the number of poles reduces the synchronous speed, slowing down the rotor. since the number of poles is necessarily an integer number, it is deduced that the speed regulation is defined in a discrete range.
- Scalar control: this control is based on voltage magnitude and frequency adjustment. An open-loop voltage frequency control provides low cost implementation but with a rough speed-torque regulation.
- Vector control: it is based on magnitude and phase of voltage or current vectors. The performance is optimal, but the costs and complexity of installation are high.

A good compromise between performance and ease of use is scalar control. It requires the installation of an inverter for frequency control and other electronic devices for voltage control.

Since the real dynamics is very complex, and no parameters (motors data, bridge and trolley masses, friction, etc) are available, during the simulation the motors are modelled with a second-order transfer function with a PID controller having as input the difference between the position set and the actual position. The constants of the transfer function and PID control have been arbitrarily defined. In any case an accurate simulation of the torque is not required.

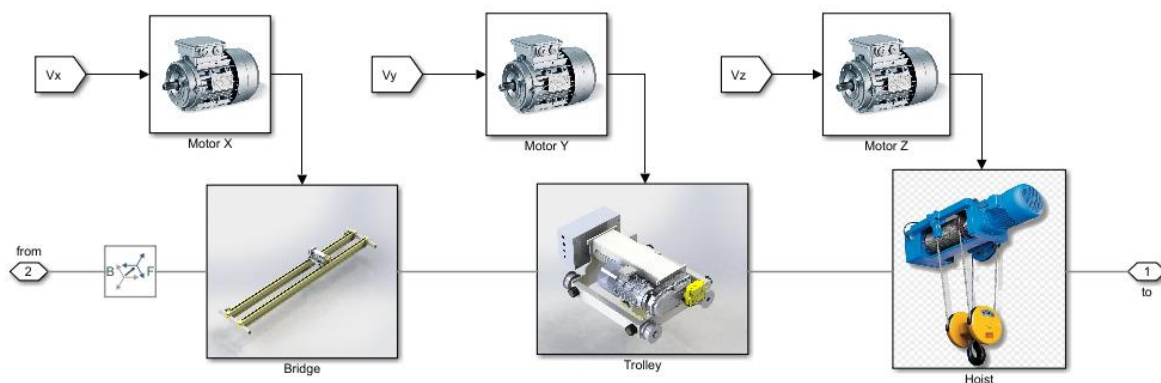


Figure 7.2: scheme of the overhead crane, hoist and hook and relative motors.

The pulley mechanism is simulated using Simscape blocks. the hypotheses valid for rope dynamics has been described in chapter 2.2.

7.1.2. Load handling device

All the components presented in paragraph 3.2 are implemented in the simulation.

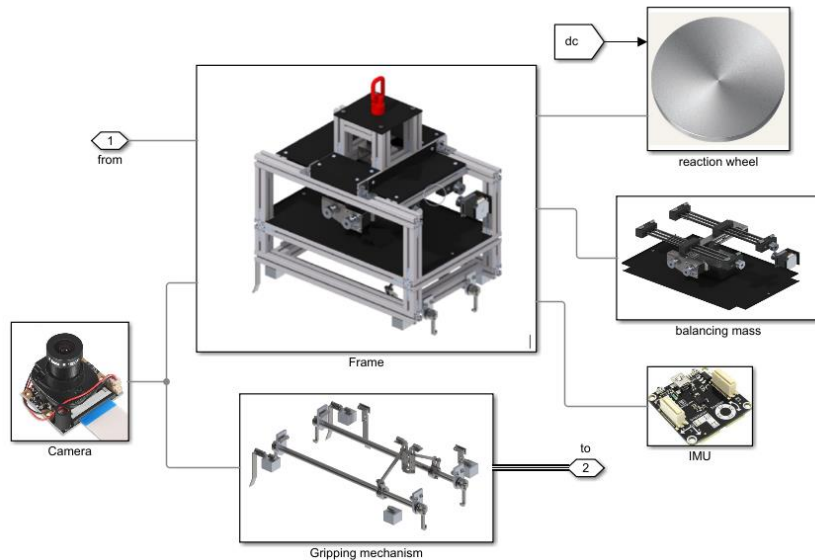


Figure 7 3: LHD components scheme.

The actuation system has the same behaviour described in figure 6.4.

The gripping and balancing mechanisms have been modelled to have a behaviour similar to the real one. the various linear actuators present have a very low operating speed; they have been modelled with a single operating speed available and a first order transfer function.

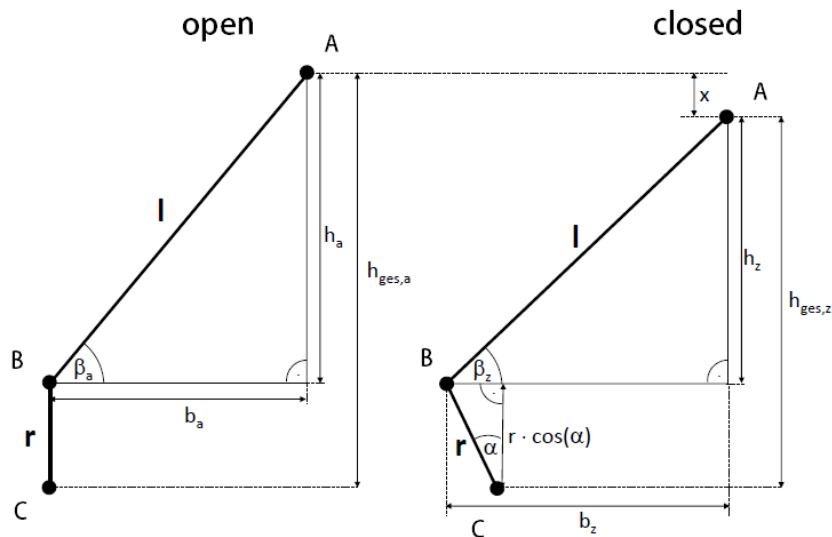


Figure 7. 4: illustration of the gripping mechanism (Fischer 2019). Point C is fixed on the frame. Point A can move along the vertical direction and the point B is a movable hinge. The linear actuator moves down and A covers the distance x . the bar l moves the point B and the bar r tilts the α angle, which is directly connected with the craft and the hooks. this mechanism is symmetrically duplicated on the right side.

7.1.3. Contact forces

The model provides for the simulation of the contact forces between the box floor and above all the contact between the hooks and the elongated holes in the box. if successful in gripping the box, it remains hanging on the gripper thanks to these forces.

7.1.4. Control logic

Control logic supervises three different blocks: the reaction wheel PID control, balancing control, and the control for the motors of the crane.

the controller gets the position of the box from an external input (for example, it is given from a human operator or from an external camera) and the trolley goes to this point.

Then, the RW PID control is activated while the IMU and the camera are operating. After 20 seconds, the hook moves down and the gripper is enabled.

The box is lifted for 20 cm above the floor, and balancing operation is enabled. At last, the hook reaches the zero position.

All the passages are resumed in (figure 7.5).

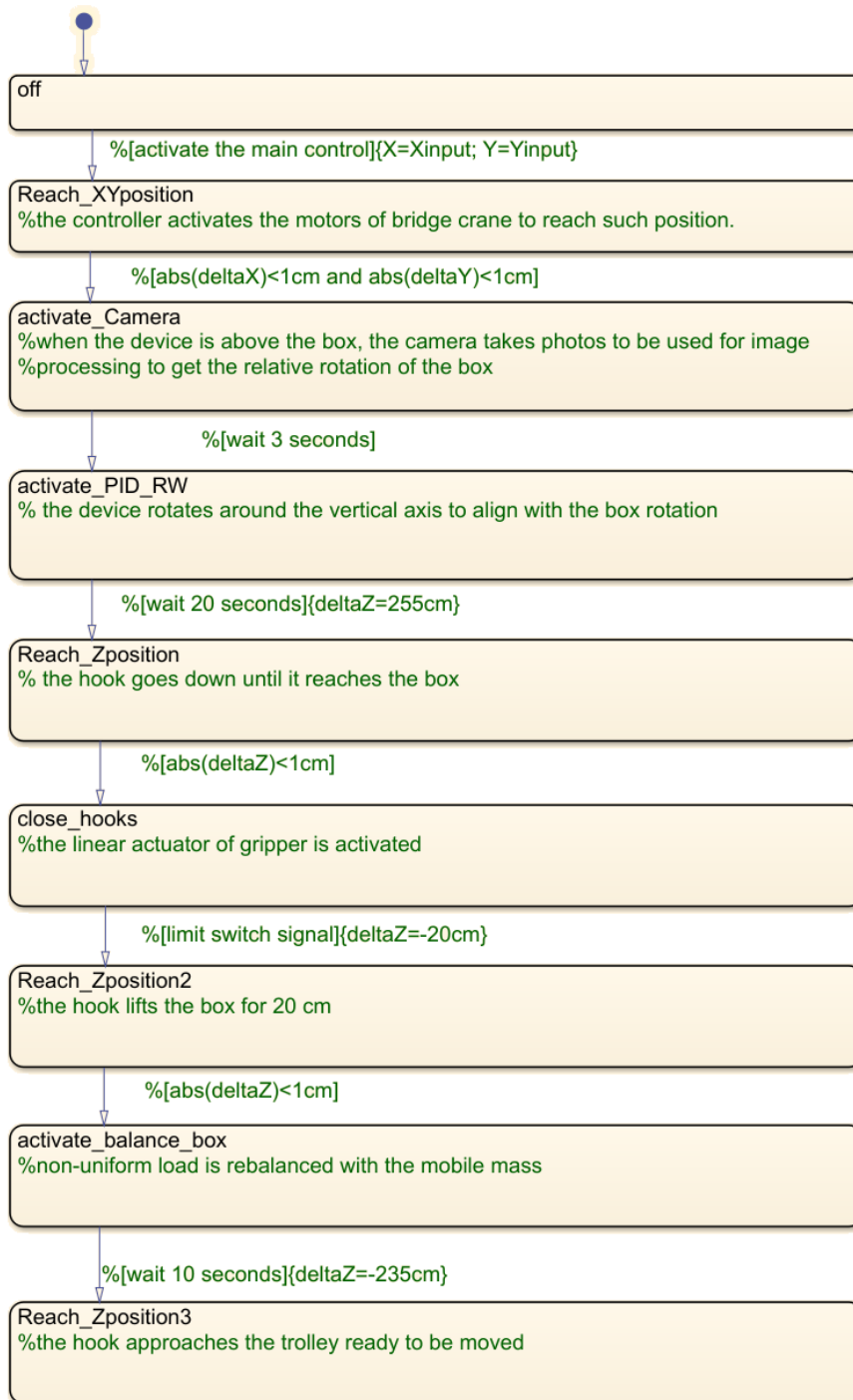


Figure 7. 5: state machine flow for main controller

Table 6.1

LHD mass	36 kg			
LHD inertia	2 kg m ²			
Hook mass	13 kg			
KLT mass	20 kg			
RW inertia	0.0175 kg m ²			
Balancing mass	11 kg			
Hook pulleys diameter	9,5 cm			
Actuator parameters				
Bridge and trolley max linear speed	25 cm/s	Relative function	Transfer	$\dot{X}, \dot{Y} = \frac{1}{s+1} v_{max}$
Hook max vertical linear speed	14 cm/s	Relative function	Transfer	$\dot{Z} = \frac{1}{0,2s+1} v_{max}$
Balance mech. Linear actuators max speed	1 cm/s	Relative function	Transfer	$\dot{x} = \frac{1}{0,1s+1} v_{max}$

7.2. Simulation results

7.2.1. Dynamics

There are two moving masses: the hook and the device. Axes X, Y and Z are referred to the inertial system reference. Y axis is oriented along the crane bridge movement, X axis is oriented along the trolley movement. The stiffness given by the four ropes is higher along the X direction than in Y direction. The joint between the hook and the ring belt gives two additional degrees of freedom to the system.

The most important result is the final relative position between point A and B. The point A is the position of the gripper in the world reference frame. Point B represents the ideal position (relative to the box) that the gripper has to reach. If A is coincident to B, correct tightening of the box is achieved.

The positioning errors are given by the relative angle θ and positions x, y, z.

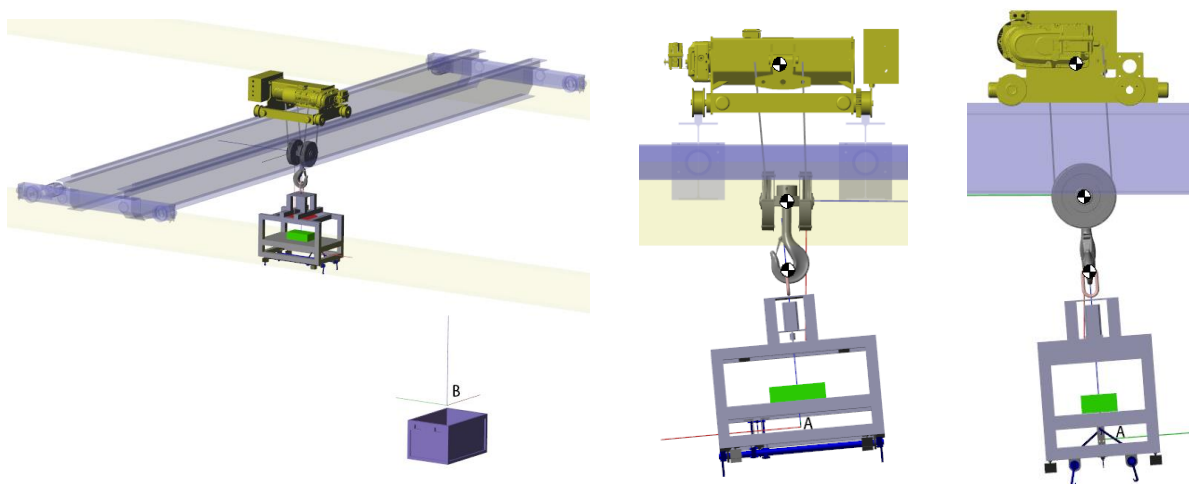


Figure 7. 6. Left: start position of the trolley. Centre: system motion along X direction. Right: system motion along Y direction. The last two figures show the hinges around which the bodies rotate.

The first simulation aims to obtain information on how far the whole system is able to approach position B. the contact forces are now disabled, so the device is free to oscillate around the final point. The position of the box is 150 cm along X direction and 200 cm along Y direction. It is rotated 90° respect to the device.

The results are shown in figure 8.4. The device reaches point B in about 38 seconds. After that time the device shows a relatively wide swing along the Y axis. in Figure 8.5, on the other hand, the swing amplitude is shown in detail. A certain drift of the y position is due to the friction in the pulley shaft on the hook, which tends to slightly shift, when the hoist is operating.

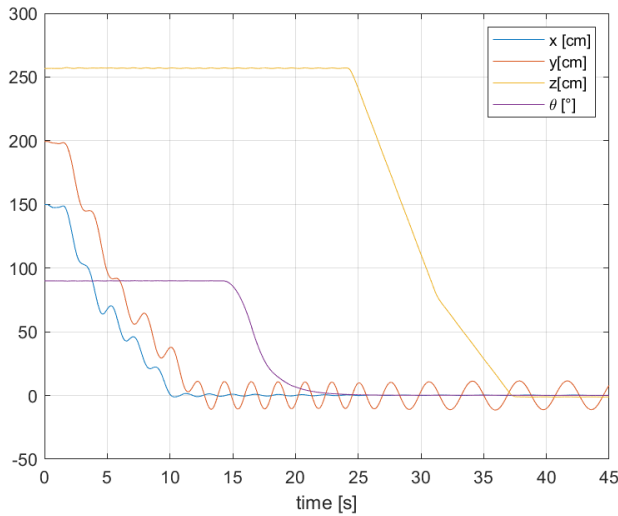


Figure 7. 7: positioning error of LHD over time.

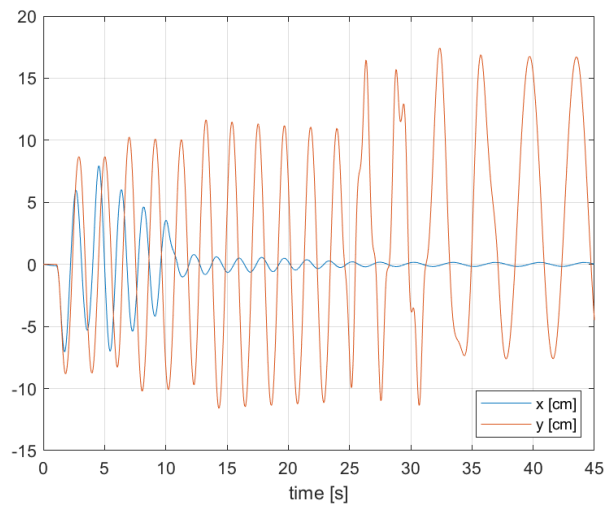


Figure 7. 8: swing of LHD along X and Y direction.

7.2.2. Balance

The balancing operation is tested. The box is placed at frame origin so the trolley does not need to move. The tilting angle is taken from the IMU. the oscillations are very high since the model is not damped. The signal is filtered with a transfer function $1/(5s+1)$ in order to take only the mean value. The box is lifted off the floor and the balancing operation starts after 34 seconds. The counterweight moves at a constant speed of 2 cm/s until the mean value of the angle is less than $0,5^\circ$; the maximum distance that the mass can reach is 15 cm. The box has a mass of 20 kg and the CoM is shifted from the geometric centre by 10 cm. This value represents the maximum value that the device is able to compensate.

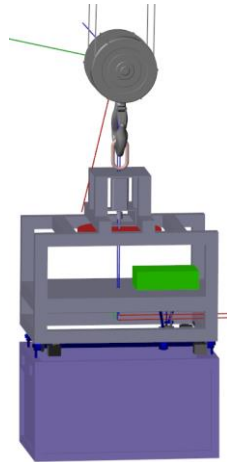


Figure 7. 9: final position of the mobile mass (green in the figure) after the balancing operation.

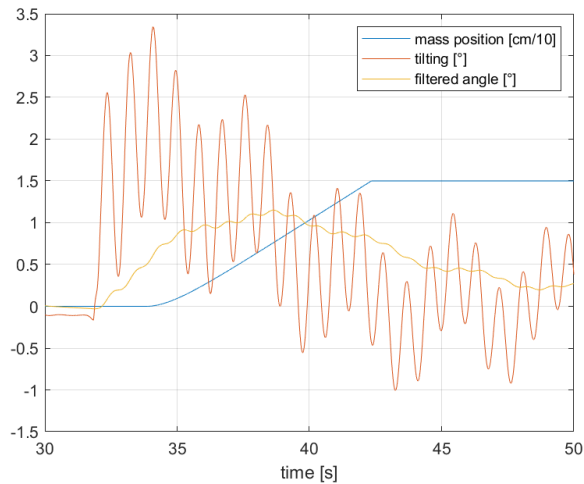


Figure 7. 10: tilting compensation of a non-uniform load (20kg and 10cm shift).

7.3. Discussion of results

The optimal positioning of the gripping mechanism with respect to the box is hampered by the swing of the device around the point. Moreover, during the simulation, many other pejorative factors were not taken into account: sensor errors, rope alignment changes during the descent phase, etc.

The most important simplification however concerns the dynamics of the bridge crane: in fact, an accuracy of positioning of the trolley with respect to the box so high could not be feasible (only few millimetres of positioning error are allowed), especially if the high mass of the bridge and the intrinsic difficulty of controlling the asynchronous motors are considered.

Irregular load balancing by means of a mobile mass has strong limits of use given by the fact that in any case the balance is limited to a low degree of balance and requires an additional mass in the device which entails a substantial deterioration of the dynamic performance and a complexity due to the installation of two series of linear actuators.

8 Swing suppression methods

The oscillation detected in the previous chapter can be explained by studying pendulum dynamics with mobile pivot. A research was conducted to identify the main methods for schematizing a bridge crane; we are in presence of an underactuated system, that is, a system in which there are more degrees of freedom than actuators.

(Hong and Shah 2019) describe three distinct methods to schematise an overhead crane:

- single pendulum model: this model represents a single rope hoisting mechanism, in which the payload and the hook are considered a unique rigid body and point-mass.
- double pendulum model: the payload has a further rotational degree of freedom (called tilting) that represents the rotation between the payload and the hook.
- multi-rope hoisting mechanism: this configuration considers multiple ropes that sustain the payload, resulting in a strongly non-linear motion. However, this mechanism increases the stiff response of the payload and a better sway suppression; as a further consequence, the inclination has a greater oscillation amplitude.

Oscillation suppression is important to ensure transport safety, prevent the payload from moving inside the box, and for positioning accuracy.

The first idea is to fix the device to the trolley during lateral movement. This requires a structural modification of the trolley and the device. Since this would require a particularly invasive modification, this approach would be appropriate with a complete replacement of the trolley. However, all the oscillations produced during the actuation of the hoist, due to friction and the movement of the ropes, would remain.

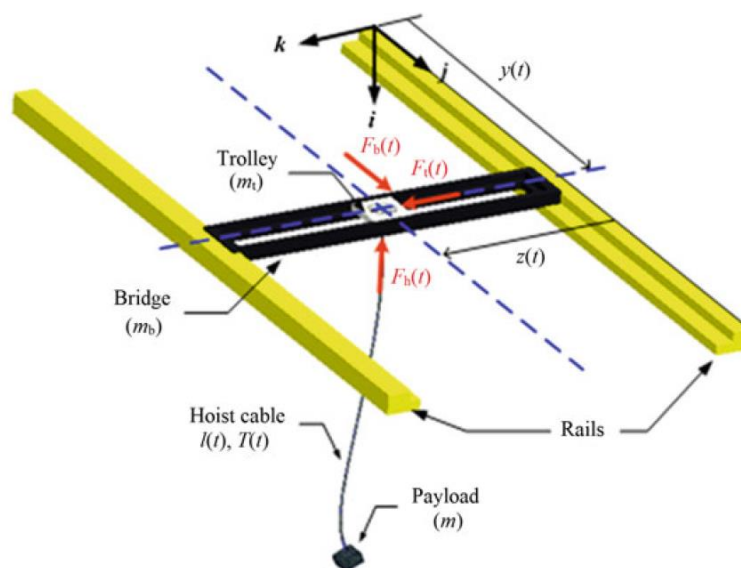


Figure 8.1: three-dimensional schematic of an overhead crane with one rope hoist (Hong and Shah 2019).

Other methods can then be used, such as the already widely used trolley anti-sway control. Other phenomena can be used such as the use of reaction wheels and gyroscopic phenomena. These methods are explained in detail in the next paragraphs.

8.1. Trolley acceleration control

This method has been widely studied in the literature. In this method, the acceleration of the trolley is used to dampen the oscillations of the pendulum.

Some anti-sway methods are described in (Dianwei 2018) and (Hong and Shah 2019). these include:

- passivity based control: it is based on the energy dissipation of the dynamic system to maintain closed-loop stability. The drawback of the method is that it requires a long of time to stabilise.
- input shaping: it is the most widely used method. It is an open-loop control that creates an input signal in order to minimize vibrations on the system. The input is composed of a series of acceleration impulses (with a consequent staircase function of the speed). to have an optimal output, it is necessary to have the frequency response of the system with respect to the control input. once this is achieved, the pulse pattern can be optimized to minimize the excitation of the system's natural frequencies. The main drawback is that, since it is an open-loop control, it is subject to parameter change errors during operation
- intelligent control like fuzzy logic, neural network based methods are used because they allow to implement a robust control without the need to obtain a mathematical model.

In paper (Rauscher, Nann and Sawodny 2018) an anti-sway control of an overhead crane with an integrated IMU on the payload is tested. The closed-loop controller is based on linear quadratic control (LQC).

The estimation of the inclination angle is provided by a Kalman filter that uses the mathematical model of the simple pendulum and the measurements from the IMU, specifically the angular velocity of the gyroscopes and the linear accelerations of the accelerometers. The Kalman filter is then coupled with a band-pass filter which eliminates both too low frequencies due to sensor bias and high frequency noise; only the frequency band around the natural frequency of the pendulum remains in the signal.

In conclusion, trolley acceleration method can be useful to limit oscillations. An optimal method would be to use hybrid controls, for example input shaping and fuzzy control, using an open-loop control to limit delay in response and a closed-loop control to increase stability and robustness.

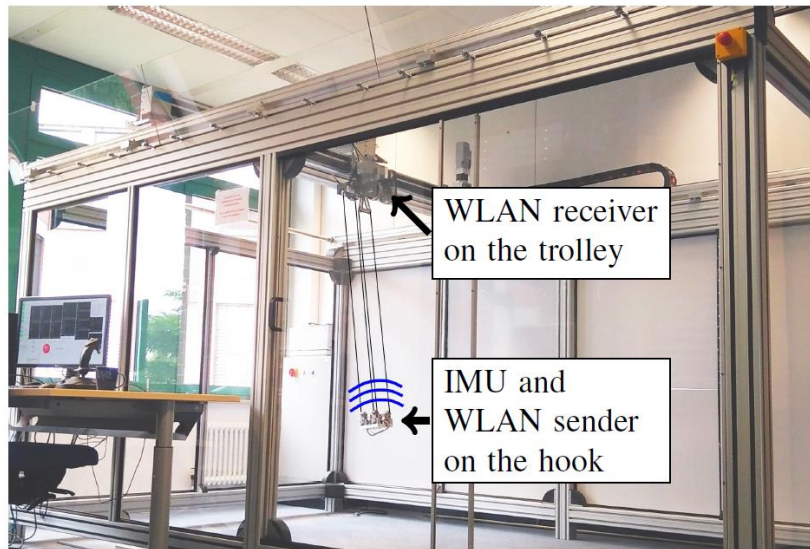


Figure 2.2: anti-sway control testbench with a hook mounted on a trolley and IMU as sensor (Rauscher, Nann and Sawodny 2018).

8.2. Lateral reaction wheel

A further RW can be placed on the frame oriented perpendicular to the main RW.

With a single pendulum model, deriving the law of motion would be trivial since an external torque would have direct action to the oscillation of the pendulum. The problem of the double pendulum is that the torque applied to the body cannot be transmitted to the main oscillation angle (in the figure 9.1 is named α), since the mobile hinge (point B in figure 9.1) is present.

Below, we will show how the dynamics of the double pendulum with RW actuation works. The equations of motion are obtained from Lagrange derivation. First, the kinetic energy and the potential energy of the double pendulum are calculated.

Generalized coordinates represent a vector able to describe each position of the body in the space, according to the constraints of the system. The minimum number of coordinates is linked to the degrees of freedom of the system.

Compared to the traditional double pendulum formulations, a different notation was preferred: the generalized coordinates are not the angles described by the ropes, but are the position x of the centre of mass of the pendulum respect to the rest position and the rotation ϕ around its principal axis of inertia respect to the vertical axis. thus, these two variables refer to an inertial coordinate system and their values can be directly sensed by the IMU. Furthermore, this guarantees that the mass matrix will subsequently be diagonal.

The potential energy is given by the gravity force, which tends to bring the system back into alignment with the vertical axis.

Once the y term is expressed using generalized coordinates, it is possible to derive the potential energy in term of x and ϕ .

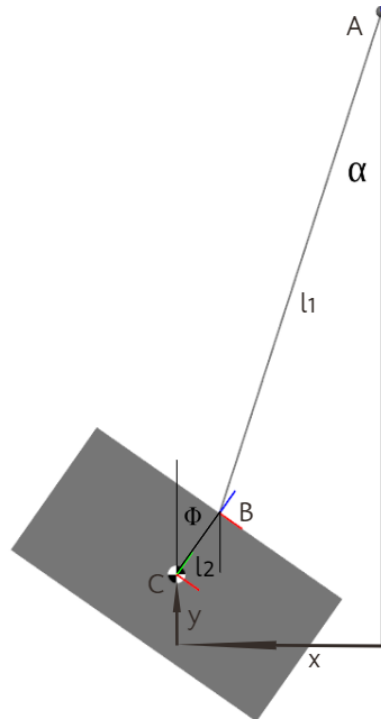


Figure 8. 3: scheme of double pendulum. Point A represents a fixed joint. Point B is a mobile joint. Point C is the centre of mass of the pendulum. l_1 is the length of the cord. l_2 is the distance between the attachment point of the rope and C. x is the horizontal distance between C and the vertical axis. y is the vertical distance between the position at rest and C.

$$\text{Kinetic energy: } T = \frac{1}{2} m \dot{x}^2 + \frac{1}{2} I \dot{\phi}^2;$$

$$\text{Potential energy: } V = mgy;$$

$$y = l_1(1 - \cos \alpha) + l_2(1 - \cos \phi)$$

$$\text{Approximation: } \cos \alpha = 1 - \frac{1}{2} \alpha^2; \cos \phi = 1 - \frac{1}{2} \phi^2;$$

$$y = \frac{1}{2} l_1 \alpha^2 + \frac{1}{2} l_2 \phi^2$$

$$x = l_1 \sin \alpha - l_2 \sin \phi$$

$$\text{Approximation: } \sin \alpha = \alpha; \sin \phi = \phi$$

$$\alpha = \frac{x}{l_1} - \frac{l_2}{l_1} \phi$$

$$y = \frac{1}{2} l_1 \left(\frac{x}{l_1} - \frac{l_2}{l_1} \phi \right)^2 + \frac{1}{2} l_2 \phi^2$$

$$V = \frac{1}{2} \frac{mg}{l_1} (x - l_2 \phi)^2 + \frac{1}{2} mgl_2 \phi^2$$

Now, using the formulation of the Lagrange equation, it is possible to derive the terms of the equations of motion.

lagrangian equation

$$\frac{d}{dt} \left(\frac{\partial L}{\partial \dot{q}_k} \right) - \frac{\partial L}{\partial q_k} = 0;$$

lagrangian definition: $L = T - V$;

generalised coordinates $\mathbf{q} = \{x, \phi\}$;

$$\frac{d}{dt} \left(\frac{\partial L}{\partial \dot{x}} \right) = m\ddot{x}; \quad \frac{d}{dt} \left(\frac{\partial L}{\partial \dot{\phi}} \right) = I\ddot{\phi};$$

$$-\frac{\partial L}{\partial x} = \frac{mg}{l_1} x - mg \frac{l_2}{l_1} \phi;$$

$$-\frac{\partial L}{\partial \phi} = mg \frac{l_2^2}{l_1} \phi - mg \frac{l_2}{l_1} x + mgl_2 \phi$$

equations of motion:

$$m\ddot{x} + \frac{mg}{l_1} x - mg \frac{l_2}{l_1} \phi = 0;$$

$$I\ddot{\phi} - mg \frac{l_2}{l_1} x + mgl_2 \left(1 + \frac{l_2}{l_1} \right) \phi = 0;$$

A RW is placed on the point C and oriented orthogonally to plane of the figure, free to rotate around its axis of symmetry. a greater weight (the weight of the wheel) will weigh on the system, but the inertia value I of the load around the centre of mass will remain unchanged.

The torque of the RW will act exclusively in the direction of coordinate ϕ .

By re-adjusting the two equations using the matrices and adding the external torque, we obtain:

$$\begin{bmatrix} m & 0 \\ 0 & I \end{bmatrix} \begin{Bmatrix} \ddot{x} \\ \ddot{\phi} \end{Bmatrix} + \begin{bmatrix} \frac{mg}{l_1} & -mg \frac{l_2}{l_1} \\ -mg \frac{l_2}{l_1} & mgl_2 \left(1 + \frac{l_2}{l_1} \right) \end{bmatrix} \begin{Bmatrix} x \\ \phi \end{Bmatrix} = \begin{Bmatrix} 0 \\ T \end{Bmatrix}$$

The torque given by the RW must now be evaluated by a control function. One possible solution is to use a dissipative control method (Brogliato, et al. 2020):

$$T = c_1 \dot{x} - c_2 \dot{\phi}$$

The couple of terms are replaced and moved to the other member of the equation. In this way, we can create a linear damping matrix:

$$\begin{bmatrix} m & 0 \\ 0 & I \end{bmatrix} \begin{Bmatrix} \ddot{x} \\ \ddot{\phi} \end{Bmatrix} + \begin{bmatrix} 0 & 0 \\ -c_1 & c_2 \end{bmatrix} \begin{Bmatrix} \dot{x} \\ \dot{\phi} \end{Bmatrix} + \begin{bmatrix} k_{11} & -k_{12} \\ -k_{21} & k_{22} \end{bmatrix} \begin{Bmatrix} x \\ \phi \end{Bmatrix} = \begin{Bmatrix} 0 \\ 0 \end{Bmatrix}$$

Table 8.1: parameters of simulation for test 1.

l1	3 m	m	40 kg	c1	307
l2	0,5 m	I	3 kg m ²	c2	26

The model on Simulink is built to verify a correspondence between the two models.

The initial values of α and ϕ are 2° . The result is shown in figure 9.2.

Setting the inertia of the RW equal to 0.0175 kg m^2 , we can evaluate the speed and the torque during the operation. As we can see, the energy contained in the pendulum swing is only transferred into the speed of the RW. At the maximum absorption capacity, the speed of RW is 10230 rpm and the maximum torque reaches 34 Nm. The time of the operation is 2 seconds.

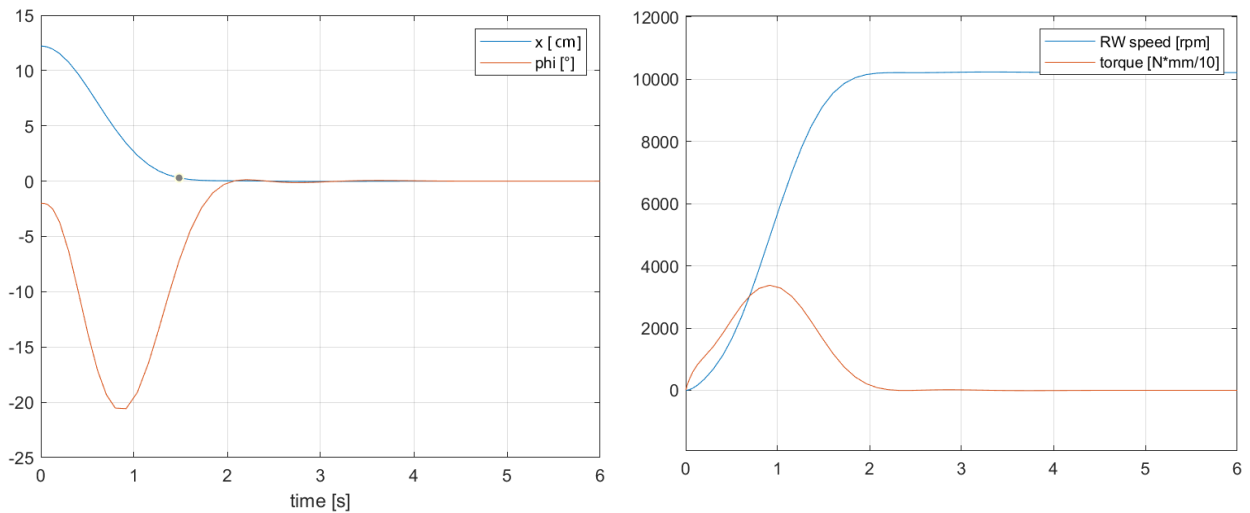


Figure 8.4: output of simulation with dissipative control (test 1).

If we consider the reaction wheel as a part of the system, we can assert that total energy is conserved. If we also want to dissipate the energy of RW, we must introduce a third dissipative component.

At this point we introduce the third equation of motion: the dissipative component c_3 concerns the speed of RW:

$$J\ddot{\gamma} = -T = c_1\dot{x} - c_2\dot{\phi} + c_3\dot{\gamma}$$

The equations are then rewritten:

$$\begin{bmatrix} m & 0 & 0 \\ 0 & I & 0 \\ 0 & 0 & J \end{bmatrix} \begin{Bmatrix} \ddot{x} \\ \ddot{\phi} \\ \ddot{\gamma} \end{Bmatrix} + \begin{bmatrix} 0 & 0 & 0 \\ -c_1 & c_2 & -c_3 \\ c_1 & -c_2 & c_3 \end{bmatrix} \begin{Bmatrix} \dot{x} \\ \dot{\phi} \\ \dot{\gamma} \end{Bmatrix} + \begin{bmatrix} k_{11} & -k_{12} & 0 \\ -k_{21} & k_{22} & 0 \\ 0 & 0 & 0 \end{bmatrix} \begin{Bmatrix} x \\ \phi \\ \gamma \end{Bmatrix} = \begin{Bmatrix} 0 \\ 0 \\ 0 \end{Bmatrix}$$

The motor speed value can be taken from an internal hall sensor. A second useful method is to realise a feedforward control for $\dot{\gamma}$: in this way, the sensor signal will no longer be needed. The following steps demonstrate the final result:

$$J\ddot{\gamma} + \frac{1}{s}c_3\dot{\gamma} = -T = c_1\dot{x} - c_2\dot{\phi}$$

$$J\ddot{\gamma} = -\frac{T}{1 + \frac{c_3}{J}\frac{1}{s}} = \frac{s}{s+h}(c_2\dot{\phi} - c_1\dot{x})$$

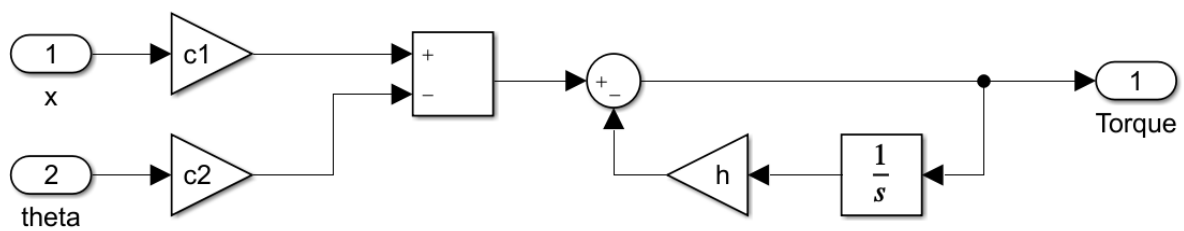


Figure 8.5: dissipative control scheme

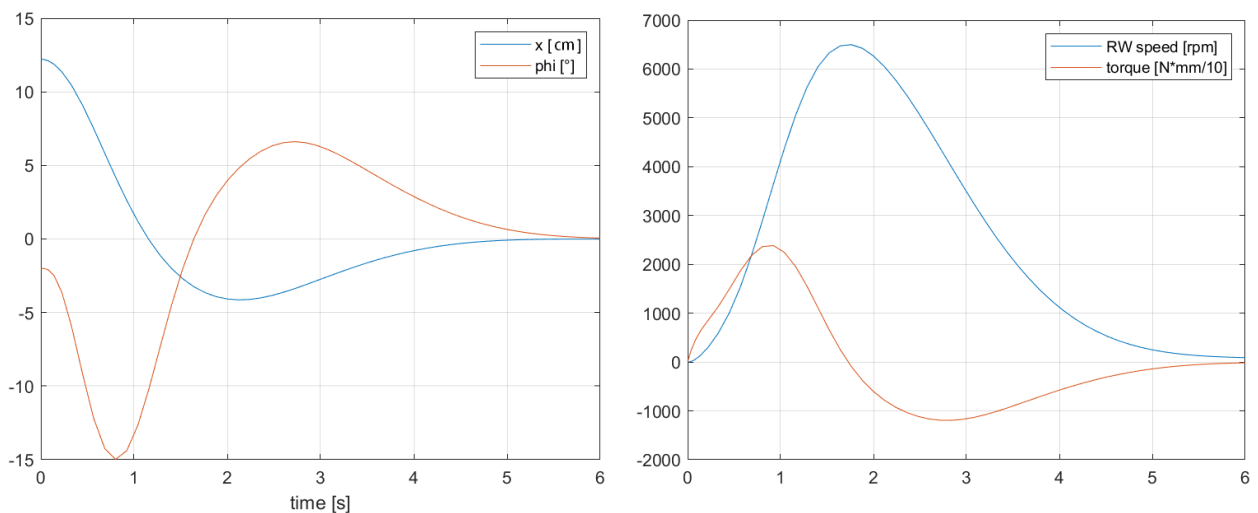


Figure 8.6: output of simulation with dissipative control including the RW (test 2).

Table 8. 2: parameters of simulation for test 2

l1	3 m	m	40 kg	c1	202 Nm/(rad/s)
l2	0,5 m	I	3 kg m ²	c2	13 Nm/(rad/s)
J	0.0175 kg m ²	h	0,59 1/s		

The new control takes more time (6 seconds) to reduce swing and tilting of the pendulum. another noteworthy fact is that the torque now has a positive direction for the first part (that corresponds to energy absorption from the pendulum) and for the second part the torque is negative, while it is braking the wheel. The maximum speed and torque are 6500 rpm and 24Nm.

Since these values of speed and torque are very difficult to reach for a motor, we then introduce saturations in the torque and speed.

A maximum torque of 1 Nm and a maximum speed of 3000 rpm is set. From results, the operation time is increased considerably (50 seconds).

The amplitude of tilting ϕ is also reduced. A motor with 1 Nm has indicatively a weight of 1,5-2 kg, and it is not convenient to increase the max torque since the weight would be too high. The dimensions of RW have been reduced to an inertia of 0.0026 kg m².

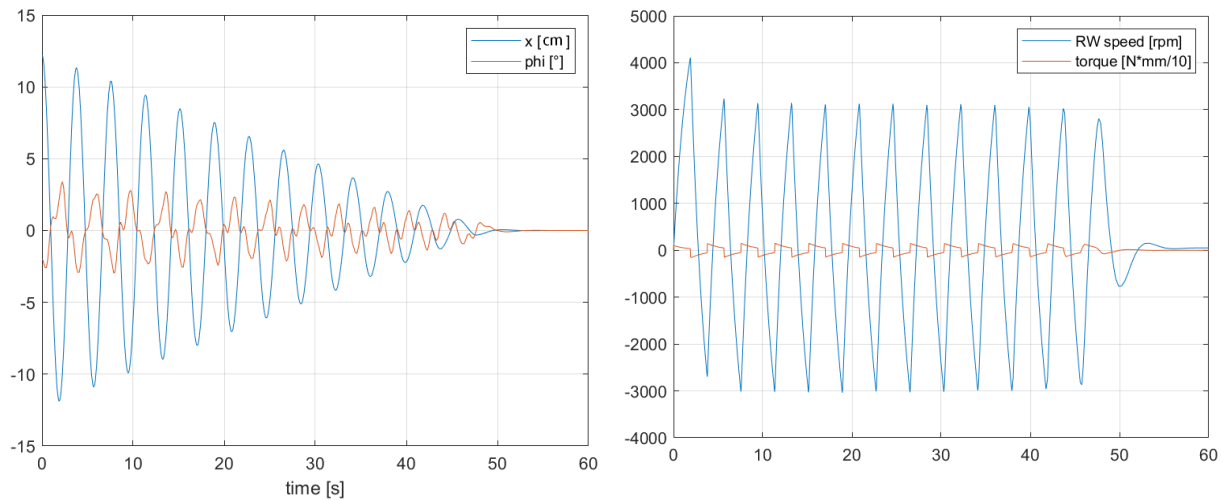


Figure 8.7: dissipative control with motor torque saturation (test 3).

8.3. single pendulum with gyroscope

Initially, the single pendulum model is presented, to observe the gyroscopic effect on a simpler model. Later, the double pendulum model will be approached using the knowledge learned in this paragraph.

The model is schematized as a pendulum with a disc, which is free to rotate along its symmetry axis, on the end of the cord suspended from a pivot.

The equations of motion are computed introducing Euler-Lagrange equation.

We have a few possibilities to choose generalised coordinates:

1. Euler angles $\mathbf{q} = \{\delta, \psi, \varphi\}$: these coordinates are commonly used to describe the spinning top motion, but they can't be used in this case because when the angle δ

is null (in the spinning top this case is not taken into consideration, whereas in our case is very common) , the vectors $\dot{\phi}$ and $\dot{\psi}$ overlap, giving rise to the gimbal lock phenomenon.

2. Use of quaternions to represent rotation $\mathbf{q} = \{a, b, c, d\}$: in this case we use four variables, so we must introduce a new equation from the definition of quaternions with Lagrange multipliers technique. The gimbal lock phenomenon is completely avoided, but the complexity of mathematical treatment is increased.
3. The angles $\mathbf{q} = \{\alpha, \beta, \varphi\}$: represents the best solution for a simple analysis of the model, especially if we consider small angles of δ (the angle between the gravity vector and the vertical axis of the flywheel). The gimbal lock now appears when δ is 90° .

we define the kinetic energy of the disc hanging on the pivot as the sum of the kinetic energy associated to the single angular velocities along the principal axes of inertia $\mathbf{J} = \{J_1, J_2, J_3\}$.

$\omega_1, \omega_2, \omega_3$ are the angular velocities along the principal inertia axes of the disc.

α, β are the axes of a fixed reference frame, and φ is oriented as ω_3 .

In order to find the expression of the kinetic energy, we must explicit the velocities $\omega_1, \omega_2, \omega_3$ in terms of α, β, φ and relative velocities along its axes, which have been chosen as generalized coordinates. The angular velocities $\dot{\alpha}, \dot{\beta}, \dot{\varphi}$ have been projected along the directions of $\omega_1, \omega_2, \omega_3$. For example, the vector $\dot{\alpha}$ has been projected onto the plane containing vectors ω_2, ω_3 by multiplying it by $\cos \beta$, namely the angle between ω_2 and $\dot{\alpha}$. After this step, we can project the resulting vector by multiplying by $\cos \varphi$. The same steps have been followed for $\dot{\beta}$. Note that the vector $\dot{\varphi}$ is always perpendicular with ω_2, ω_3 , so the contribute for these vectors is null. Finally we add the resulting vectors and the result is: $\omega_2 = \dot{\alpha} \cos \beta \cos \varphi - \dot{\beta} \cos \alpha \sin \varphi$. With the same approach we can find the expressions for ω_1 and ω_3 .

The potential gravitational energy V only depends on the displacement Δy of the center of mass m along the gravity direction:

$$V = mg \cdot \Delta y = mg \cdot l(1 - \cos \delta) = mg \cdot l(1 - \cos \alpha \cos \beta)$$

Where l is the length of the cord.

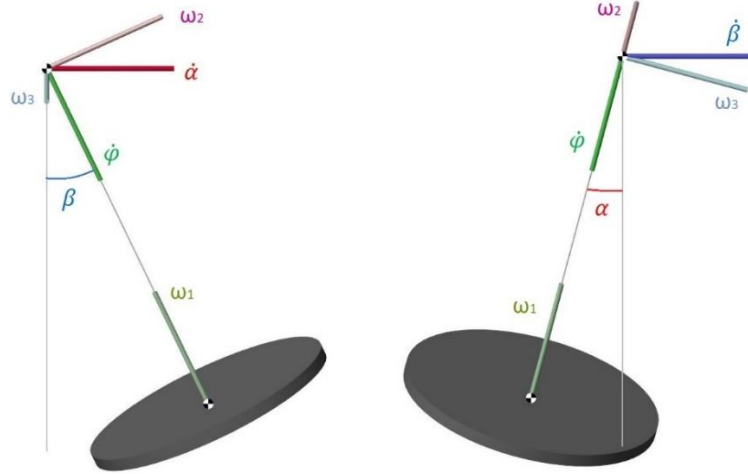


Figure 8.8: model of the flywheel suspended by the cord.

lagrange equations:

$$\frac{d}{dt} \left(\frac{\partial L}{\partial \dot{q}_k} \right) - \frac{\partial L}{\partial q_k} = 0;$$

$$\text{lagrangian: } L = T - V;$$

generalized coordinates: $\mathbf{q} = \{\alpha, \beta, \varphi\}$

$$\text{Kinetic energy: } T = \frac{1}{2} \dot{\mathbf{q}} \cdot \mathbf{J} \cdot \dot{\mathbf{q}} = \frac{1}{2} J_1 \omega_1^2 + \frac{1}{2} J_2 \omega_2^2 + \frac{1}{2} J_3 \omega_3^2$$

$$\omega_1 = \dot{\varphi} - \dot{\beta} \sin \alpha + \dot{\alpha} \sin \beta$$

$$\omega_2 = \dot{\alpha} \cos \varphi \cos \beta - \dot{\beta} \sin \varphi \cos \alpha$$

$$\omega_3 = \dot{\alpha} \cos \varphi \cos \beta + \dot{\beta} \cos \varphi \cos \alpha$$

if $J_2 = J_3$ then:

$$\omega_2^2 + \omega_3^2 = \dot{\alpha}^2 \cos^2 \beta + \dot{\beta}^2 \cos^2 \alpha$$

renaming $J_2 = J_3 = I$ and $J_1 = J$ and replacing:

$$T = \frac{1}{2} J (\dot{\varphi} - \dot{\beta} \sin \alpha + \dot{\alpha} \sin \beta)^2 + \frac{1}{2} I (\dot{\alpha}^2 \cos^2 \beta + \dot{\beta}^2 \cos^2 \alpha)$$

$$\text{potential energy: } V = mgl \cdot (1 - \cos \alpha \cos \beta)$$

$$\text{approximations: } \sin \alpha = \alpha, \sin \beta = \beta, \cos \alpha = 1 - \frac{1}{2} \alpha^2, \cos \beta = 1 - \frac{1}{2} \beta^2$$

$$T = \frac{1}{2} J (\dot{\varphi} - \dot{\beta} \alpha + \dot{\alpha} \beta)^2 + \frac{1}{2} I (\dot{\alpha}^2 + \dot{\beta}^2)$$

if we neglect the infinitesimals of second order:

$$T = \frac{1}{2} J (\dot{\varphi}^2 - \dot{\varphi} \dot{\beta} \alpha + \dot{\varphi} \dot{\alpha} \beta) + \frac{1}{2} I (\dot{\alpha}^2 + \dot{\beta}^2)$$

$$\frac{\partial L}{\partial \dot{\alpha}} = \frac{1}{2} J \dot{\varphi} \beta + I \dot{\alpha}$$

$$\frac{d}{dt} \left(\frac{\partial L}{\partial \dot{\alpha}} \right) = \frac{1}{2} J \ddot{\varphi} \beta + \frac{1}{2} J \dot{\varphi} \dot{\beta} + I \ddot{\alpha} = \frac{1}{2} J \dot{\varphi} \dot{\beta} + I \ddot{\alpha}$$

$$\frac{\partial L}{\partial \dot{\beta}} = -\frac{1}{2} J \dot{\varphi} \alpha + I \dot{\beta}$$

$$\frac{d}{dt} \left(\frac{\partial L}{\partial \dot{\beta}} \right) = -\frac{1}{2} J \ddot{\varphi} \alpha - \frac{1}{2} J \dot{\varphi} \dot{\alpha} + I \ddot{\beta} = -\frac{1}{2} J \dot{\varphi} \dot{\alpha} + I \ddot{\beta}$$

$$\frac{\partial L}{\partial \alpha} = -\frac{1}{2} J \dot{\varphi} \dot{\beta} - mgl \sin \alpha \cos \beta \cong -\frac{1}{2} J \dot{\varphi} \dot{\beta} - mgl \alpha$$

$$\frac{\partial L}{\partial \beta} = \frac{1}{2} J \dot{\varphi} \dot{\alpha} - mgl \cos \alpha \sin \beta \cong \frac{1}{2} J \dot{\varphi} \dot{\alpha} - mgl \beta$$

$$\frac{d}{dt} \left(\frac{\partial L}{\partial \dot{\varphi}} \right) = \ddot{\varphi}, \quad \frac{\partial L}{\partial \varphi} = 0$$

Equations of motion:

$$I \ddot{\alpha} + J \dot{\varphi} \dot{\beta} + mgl \alpha = 0;$$

$$I \ddot{\beta} - J \dot{\varphi} \dot{\alpha} + mgl \beta = 0$$

$$\ddot{\varphi} = 0$$

A new model has been composed in Simulink and compared with the equations of the approximated model in Simulink. The output values are the angles α and β . We can notice that the accuracy of our model decreases with increasing of the initial angle.

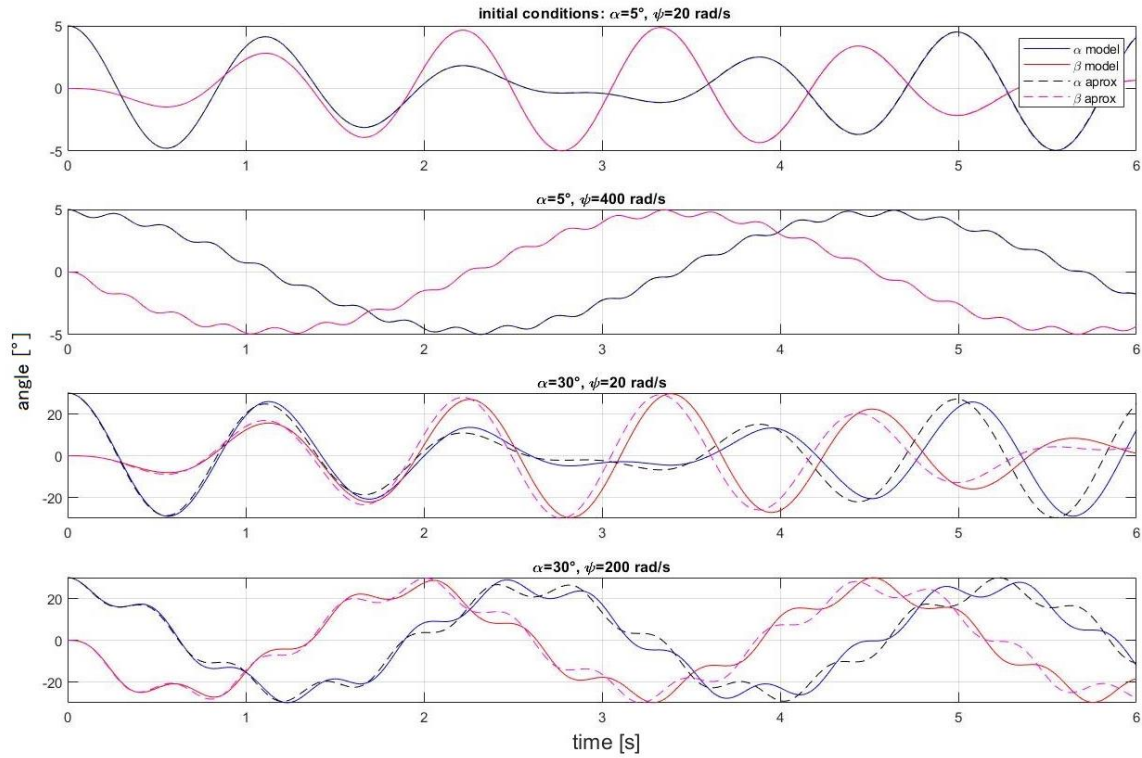


Figure 8.9: comparison between Simulink model output and the linear equation results.

Now, we can add the payload with inertia J_p (around the vertical axis) to the model: a new coordinate θ that represents the displacement of the payload is added and φ is renamed as the relative displacement between the payload and the reaction wheel. J is also renamed as J_w . The total mass, the distance l between the center of mass and the pivot and the inertia I are recalculated with the additional mass. The equations are written below:

$$I\ddot{\alpha} + J_w(\dot{\theta} + \dot{\varphi})\dot{\beta} + J_p \dot{\theta} \dot{\beta} + mgl \alpha = 0$$

$$I\ddot{\beta} - J_w(\dot{\theta} + \dot{\varphi}) \dot{\alpha} - J_p \dot{\theta} \dot{\alpha} + mgl \beta = 0$$

$$J_w(\ddot{\theta} + \ddot{\varphi}) + J_p \ddot{\theta} = 0$$

The equations can be rewritten as:

$$I\ddot{\alpha} + (J_w \dot{\varphi} + (J_p + J_w) \dot{\theta}) \cdot \dot{\beta} + mgl \alpha = 0$$

$$I\ddot{\beta} - (J_w \dot{\varphi} + (J_p + J_w) \dot{\theta}) \cdot \dot{\alpha} + mgl \beta = 0$$

$$J_w \dot{\varphi} + (J_p + J_w) \dot{\theta} = \text{constant}$$

We can notice that an exchange of internal forces between the RW and the payload doesn't affect the gyroscopic torque resulting along the direction of axes α and β , since the sum of the angular momentum remains constant.

We can approximate the inertia along the axes α and β as a point mass. That means: $I = m l^2 + I_0 \cong m l^2$, where I_0 is the inertia calculated around the centre of mass. It is true if the cord is long enough. So we can rename the sum $J_w + J_p$ as I and J_w as J .

$$m l^2 \ddot{\alpha} + (J \dot{\phi} + I \dot{\theta}) \cdot \dot{\beta} + m g l \alpha = 0$$

$$m l^2 \ddot{\beta} - (J \dot{\phi} + I \dot{\theta}) \cdot \dot{\alpha} + m g l \beta = 0$$

$$J \dot{\phi} + I \dot{\theta} = \text{constant} = q$$

8.4. Double pendulum with gyroscope

to implement the linear model of the double pendulum with gyroscopic effect, we follow an easier way than solving the Lagrange equations from scratch, that is, we join the model of the double pendulum used in equations 9 by adding the gyroscopic torque found in equations 9.

the equation 9 must be extended in a three-dimensional system, so we will have a system of equations in four dimensions: x_1 and ϕ_1 along direction of α , x_2 and ϕ_2 along direction of β . Without the gyroscopic torques, two systems are independent from each other. the inertias I_1, I_2 along ϕ_1, ϕ_2 are different if the shape of the frame is not symmetrical between the two planes. the values of the stiffness matrix have the same meaning presented in eq 9.

it can be said that the gyroscopic torque acts in the directions of ϕ , exactly as with the moment of RW in equation 9. We can now write the equations of motion in the matrix form:

$$\begin{bmatrix} m & 0 & 0 & 0 \\ 0 & I_1 & 0 & 0 \\ 0 & 0 & m & 0 \\ 0 & 0 & 0 & I_2 \end{bmatrix} \begin{Bmatrix} \ddot{x}_1 \\ \ddot{\phi}_1 \\ \ddot{x}_2 \\ \ddot{\phi}_2 \end{Bmatrix} + \begin{bmatrix} 0 & 0 & 0 & 0 \\ 0 & 0 & 0 & q \\ 0 & 0 & 0 & 0 \\ 0 & -q & 0 & 0 \end{bmatrix} \begin{Bmatrix} \dot{x}_1 \\ \dot{\phi}_1 \\ \dot{x}_2 \\ \dot{\phi}_2 \end{Bmatrix} + \begin{bmatrix} k1 & -k2 & 0 & 0 \\ -k2 & k3 & 0 & 0 \\ 0 & 0 & k1 & -k2 \\ 0 & 0 & -k2 & k3 \end{bmatrix} \begin{Bmatrix} x_1 \\ \phi_1 \\ x_2 \\ \phi_2 \end{Bmatrix} = \begin{Bmatrix} 0 \\ 0 \\ 0 \\ 0 \end{Bmatrix}$$

The final effect of the gyroscopic moment on the pendulum is to transfer the oscillation energy from direction x_1 to orthogonal direction x_2 , as can be seen from figure 9.2. The total energy is conserved, as it was clear from the fact that there are no external forces or dissipative forces. The data are the same described in table 9.1; I_1 and I_2 have the same value; the wheel has a speed of 6000 rpm and inertia 0.0175 kg m^2 . The value of q is then $11 \text{ Nm}/(\text{rad/s})$.

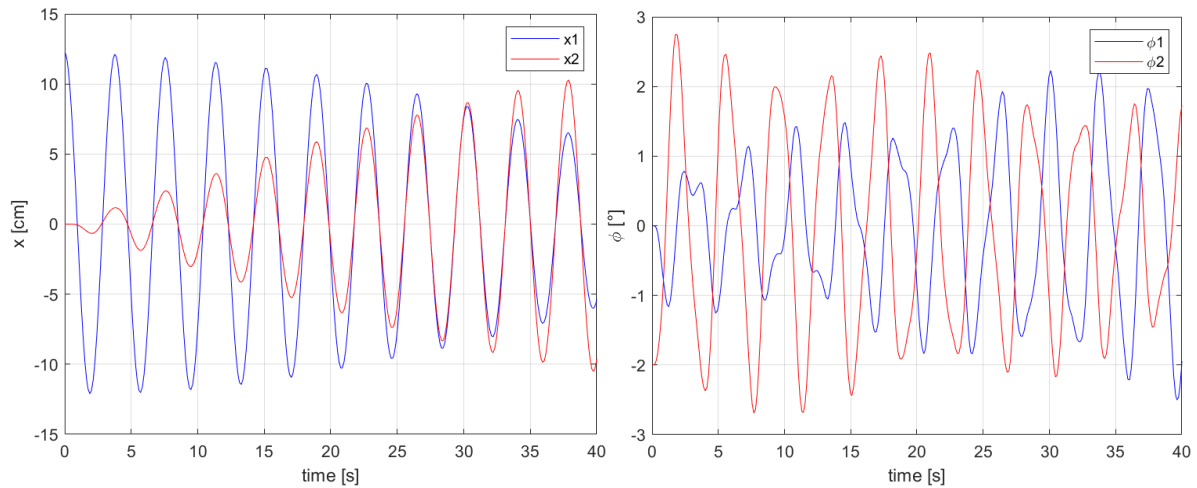


Figure 8.10: gyrosopic effect on double pendulum.

The possibility of controlling the device by inserting a motor to control the axis of the gyroscope was investigated.

The attempt was unsuccessful, due to the complexity of the nature of the gyrosopic momenta on a body with 6 degrees of freedom. In order for this type of control to be effective, the number of degrees of freedom should be reduced; for example, making one of the pendulum swing directions infinitely rigid and the q term acting as a linear damping.

Another control method is to couple two gyroscopes that rotate in the opposite direction. this control is called scissored-pair control moment gyroscope system. The coupling of opposite spinning flywheels has the advantage of isolating the output torque to a single axis, where off-axis torques are cancelled out (Chiu and Goswami 2014). The torque is managed by a single stepper motor that changes the orientation of the flywheels. To obtain the resulting torque along the desired direction, gymbal axes of two flywheels must rotate in the opposite direction, using a gear mechanism. The control system is already in use for spacecrafts or for the stabilisation of mechanisms schematised as inverted pendulums.

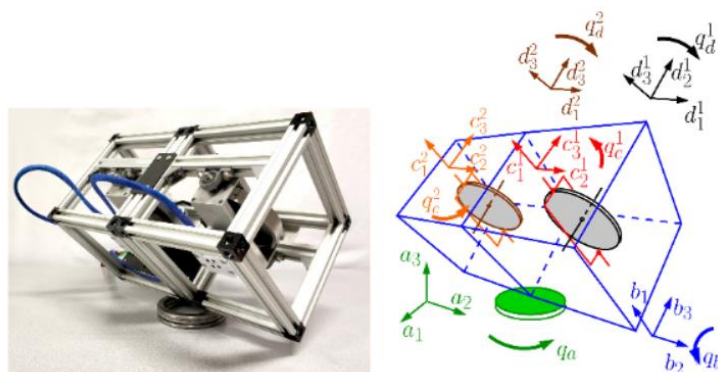


Figure 8.11: prototype of a scissored-pair control moment gyroscope system studied for the stabilisation of a rigidbody placed on a thrust bearing (Aranovskiy, et al. 2020)

9 Positioning accuracy improvements

An idea that could prove successful is to provide the gripping mechanism with a further translation movement relative to the device.

This system would allow to have a very high precision within a limited range, without the need to move the trolley. The range must be calculated to cover the positioning uncertainty of the trolley.

Technical details of the construction will not be discussed in the thesis. In the model, the old gripping mechanism with lateral movement will be equipped with two groups of linear actuators to enable lateral displacements. The simulation aims to show the possible use of this feature and simulate the dynamics.

Two operating modes can be implemented: the balancing operation, originally entrusted to the mobile counterweight, and the displacement of the CoM of the payload during pick-up and release of the box.

9.1. Dynamics

The dynamics of a relative movement of the box respect to the device is analysed. In figure 8.9 the scheme of the mechanism is drawn. The function of the mechanism is to move the box with respect to the vertical rest position thanks to the counterweight of the device.

The variables and geometric parameters are defined as follows, using the definition of points A, B, C,D, E from figure 8.9:

- x_1, x_2 are the distance of centres of mass from the vertical position.
- $l_1 = \overline{AB}, l_2 = \overline{DE}$; the two segments both form the same angle ϕ with the vertical axis.
- $\Delta x = \overline{CD}$ is the relative movement of linear actuator. such segment is perpendicular to l_1 and l_2 .

The input of the system is Δx ; the output is the x_2 . Three equations describe the mechanism. The first one involves the equilibrium of the moments of gravity forces around the fixed joint A:

$$m_1 g x_1 = m_2 g x_2$$

the other two involve geometric relationships:

$$\Delta x = L \sin \phi + x_2 + l_2 \sin \phi \cong L \phi + x_2 + l_2 \phi$$

$$x_1 = l_1 \sin \phi \cong l_1 \phi$$

The trigonometric functions are linearised to simplify the treatment.

We have three variables (ϕ, x_2, x_1) and three equations, so the system is defined. x_2 is now expressed in terms of Δx :

$$\begin{aligned}
 x_2 &= \Delta x - L \phi - l_2 \phi \\
 x_1 &= \frac{m_2}{m_1} x_2 \\
 \phi &= \frac{x_1}{l_1} = \frac{m_2}{m_1 l_1} x_2 \\
 x_2 + L \left(\frac{m_2}{m_1 l_1} x_2 \right) + l_2 \left(\frac{m_2}{m_1 l_1} x_2 \right) &= \Delta x \\
 x_2 &= \frac{l_1 m_1}{l_1 m_1 + L_1 m_2 + l_2 m_2} \cdot \Delta x
 \end{aligned}$$

The best response is obtained when $L_1 m_2 + l_2 m_2$ is negligible compared to $l_1 m_1$.

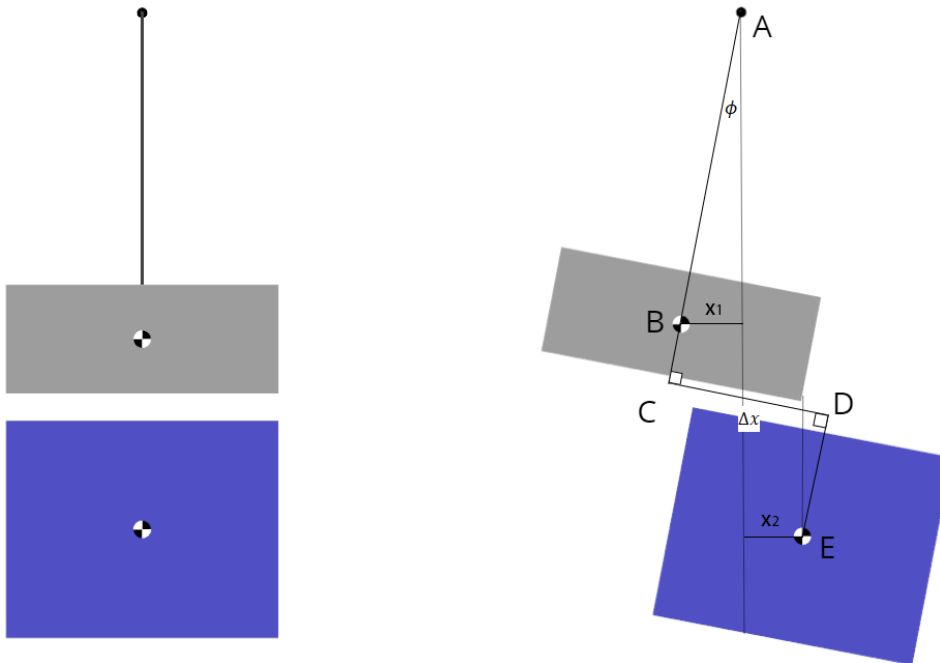


Figure 9.1. Left: rest position. Right: effect of the linear actuator on the system geometry. A is a fixed joint which corresponds to the attachment point between the hook and the device. B and E are the centres of mass of two bodies. C and D are the extremes of the actuator.

9.2. Balancing operation

The balancing operation involves reducing the tilt angle when the box has an unbalanced load.

In the initial instant, the load is aligned with the device forming a tilt angle. the load was then moved by moving its centre of mass towards the vertical axis. the same thing happens for the mass of the device. finally, the two centres of mass will be exactly aligned with the vertical axis.

This balancing operation is more efficient, for the following reason: no mass is added to act as a counterweight; on the contrary, the entire mass of the frame is used as a counterweight. The system is particularly effective with a relatively high weight with reduced lever arm of the weight force because this system allows to automatically align the centre of gravity with the vertical axis. in the case of high lever arms with low weights, then the weight of the frame allows to counterbalance the weight.

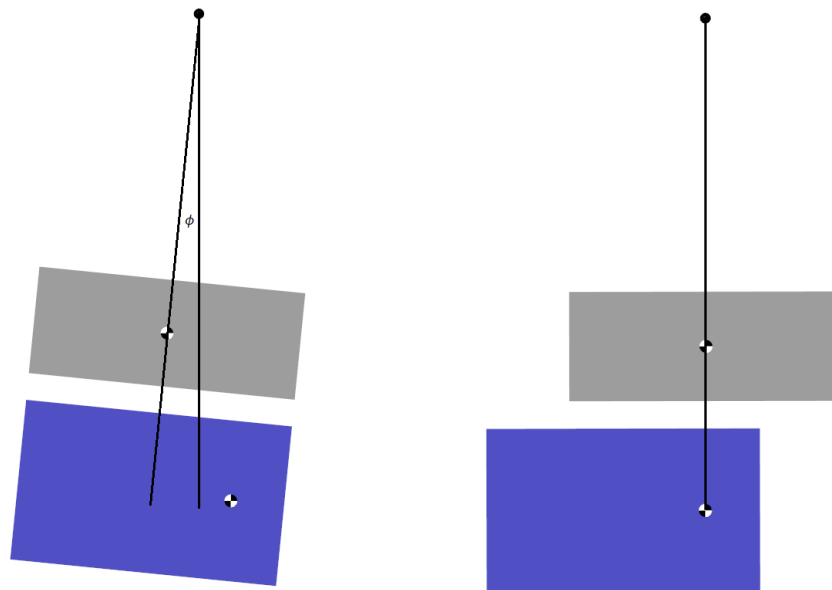


Figure 9. 2: operation of the linear actuator to reduce the tilt angle.

9.3. tilt angle compensation

With regard to the gripping operation, the gripping mechanism is the mass to be moved. In this case it can be noted that the mass is small with respect to the entire frame and that the length l_2 is almost zero.

The dynamic response is optimal, because the relative displacement of the gripping mechanism with respect to the vertical position x_2 is almost equal to the relative displacement of the actuator Δx ; furthermore, the tilt angle ϕ is tolerably low.

The main problem occurs in the stacking phase of the box because the mass is approximately equal to the frame mass and the length l_2 is considerable. This translates into a high ϕ value (tilt angle) and a shorter x_2 value.

We can continue to investigate a method to solve the problems mentioned. The first more intuitive option is to provide the gripping mechanism with a rotary motion around its axis, in order to compensate for the tilt angle. This type of rotation must also be allowed along the two directions. A solution could be to introduce four linear actuators in the four corners of the device. To obtain rotation of the box, it is necessary to extend a pair of actuators. The actuators are connected to the bodies by means of revolute joints. The result is shown in figure 9.3.

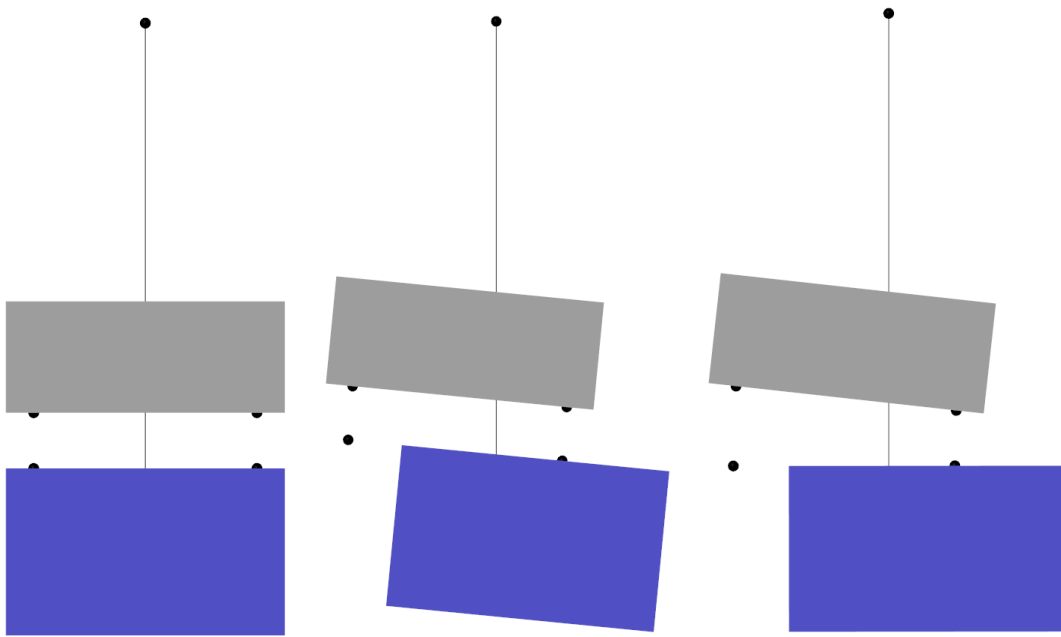


Figure 9.3: operation of the linear actuators (the extremities are marked by a black dot) for tilt angle compensation

The actuators start from the minimum length position and are blocked. The rotation of the box occurs thanks to the extension of the actuators opposite to the distance x_2 . the advantages of this arrangement are manifold: in this way the greater force always goes on the locked actuators, because the centre of mass is moved towards them, and the mobile actuators are benefited by the fact that the force of gravity has the same direction of the desired motion, they must just stop the fall. The electrical actuation would only serve to return the mechanism to its initial position when the box was released.

This system can replace also the displacement used for the balance operation. The advantage is that the weight is better distributed on the structure.

Different solutions of how to place the actuators are possible, according to the construction requirements. For example, an alternative solution is presented in figure 9.4. In this design the actuators are positioned above the frame and move it

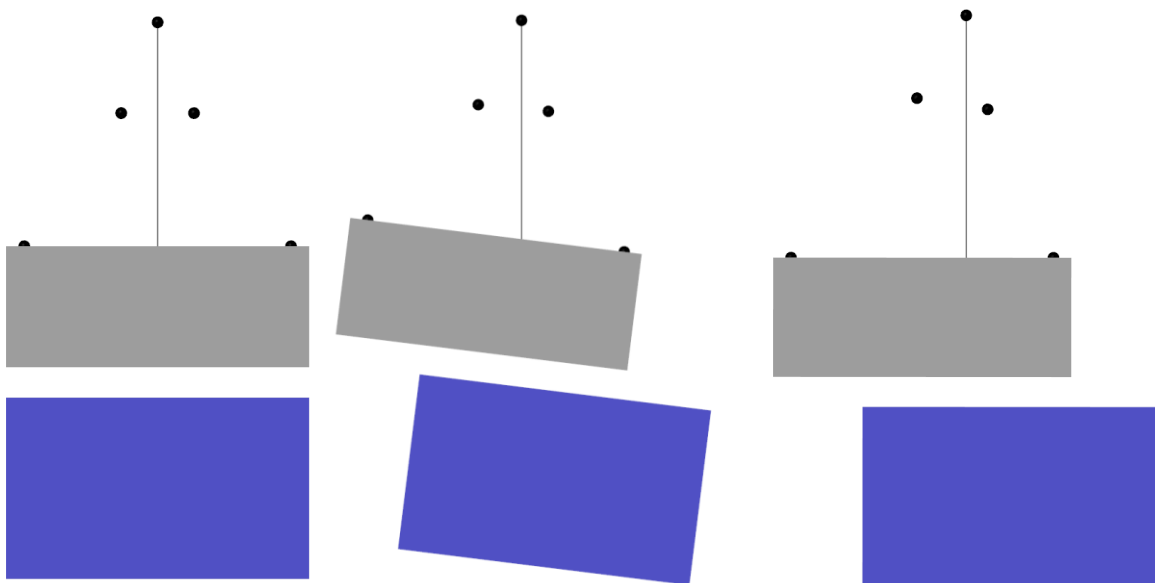


Figure 9.4: new design for tilt angle compensation

A cheaper solution could be implemented using a mechanism with cables and pulleys. the figure explains a possible configuration. The main frame is supported by cables with pulleys on a metal plate which has the swivel hook for rotary movement along the vertical axis.

The cable layout has been optimized for greater rigidity. In fact, the attachment points are distributed so as to avoid a deflection of the frame. Four central cables support most of the weight, while the lateral cables provide rigidity for lateral displacements.

Actuation is provided by four stepper motors (visible in red in the figures) mounted on the innermost pulleys. The rotation of the latter, in fact, allows the unwinding of the cable allowing the elongation of one side with respect to the other. the pulley system also has the purpose of reducing the torque required by the actuator.

The model was designed on Solidworks and implemented on Simulink for dynamic analysis. it is therefore possible to simulate the movement of the pulleys to observe the actual functionality of the mechanism.

The driving pulley contains a system that allows to fix the end of the rope avoiding the relative sliding.

The diameter of the driving pulley must have a diameter value sufficient to contain the elongation of the rope to compensate the angle with a rotation less than 360° , otherwise a pulley should be grooved in order to avoid overlapping with the outgoing rope.

In the simulation, the diameter used for the driving wheel is 60 mm, which is sufficient to contain the angle within 204° for a $75\text{ mm } x_2$ movement.

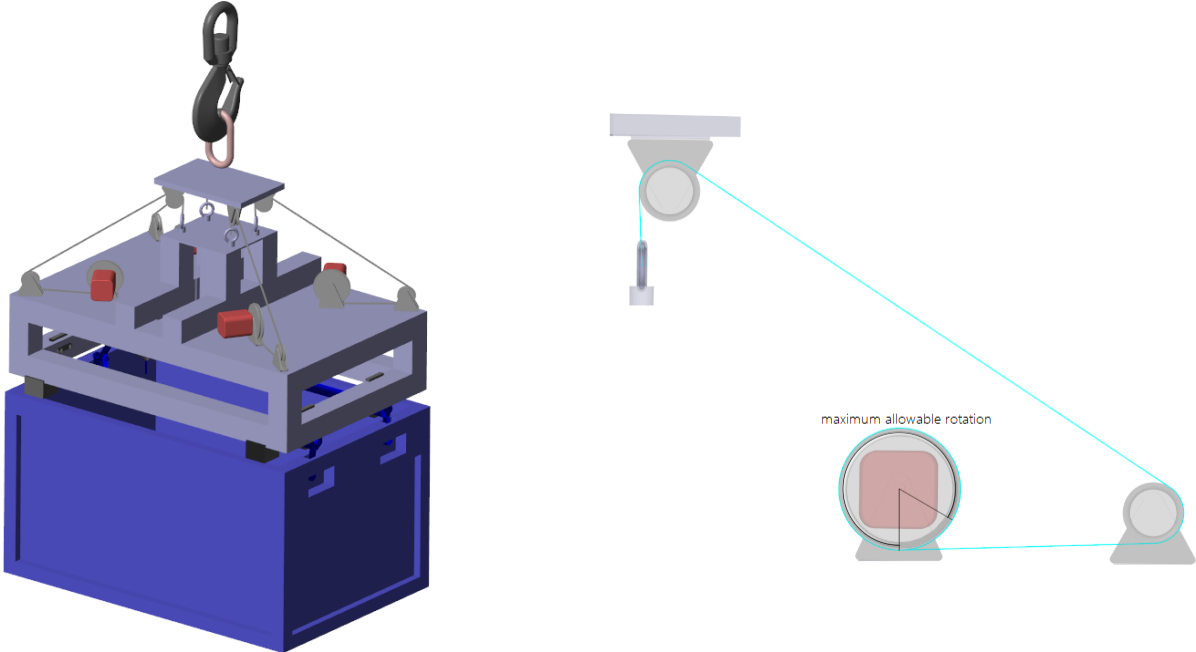


Figure 9.5. Left: overall design of new concept. Left: detail of one of the four pulley rope mechanisms with normal view on the plane of sliding of the rope. the maximum rotation amplitude that the driven pulley can cover is visible.

At the end of the operation, it is noted that the ropes are misaligned with respect to the starting point. In addition, the weight force now weighs more heavily on the right pulleys. In conclusion, a diagonal load shift is tested. the box is moved 75 mm along the x direction and 50 mm along the y direction. The tilt angle control acts first on the inclination along x and then on the inclination along y. the simulation shows that the control is feasible. The pulley that must travel the maximum rotation is the one located in the opposite corner to the movement of the box. its value is highlighted in the table and is below the maximum value.

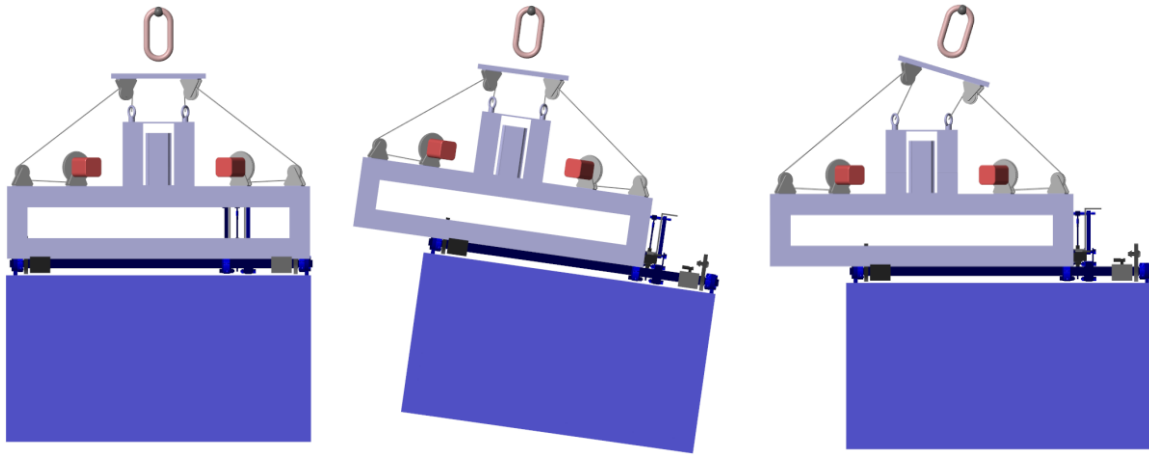


Figure 9.6: operation of the mechanism for tilt angle compensation of a lateral displacement.

Table 9. 2: simulation parameters and results for a lateral displacement.

Box mass	20 kg	Frame mass	20 kg
Actuator displacement	150 mm	Resulting tilt angle	8°
Driving pulley primitive diameter	60 mm	Driving pulley rotation	204°
Driven pulley prim. diameter	30 mm	rope elongation	107 mm
x ₂ before tilt compensation	47 mm	x ₂ after tilt compensation	75 mm

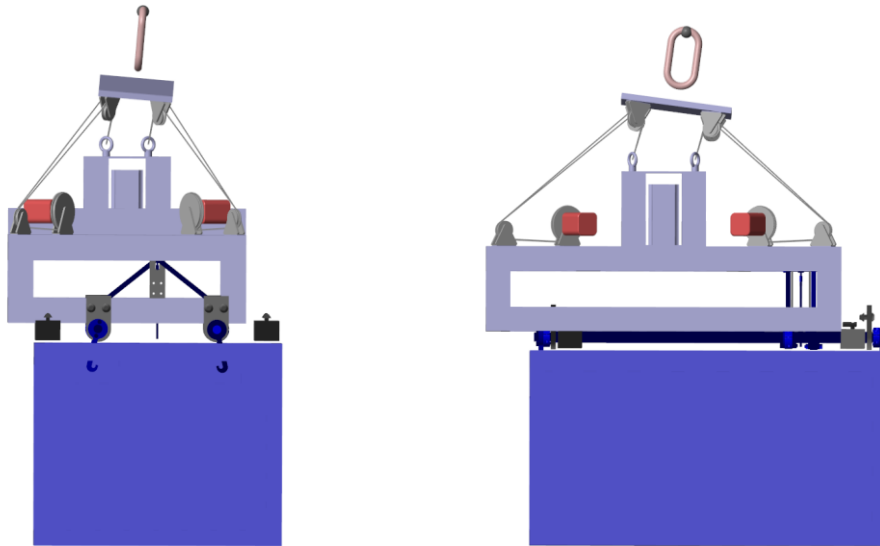


Figure 9.7: front and side view of the device after the tilt angle compensation for a diagonal displacement.

Table 9. 3: simulation parameters and results for a diagonal displacement.

Box mass	20 kg	Frame mass	20 kg
Actuator displacement along x	75 mm	Resulting tilt angle (x dir.)	4°
Actuator displacement along y	50 mm	Resulting tilt angle (y dir.)	2.7°
Driving pulley primitive diameter	60 mm	Driv. pulley max rotation	135°
Driven pulley prim. diameter	30 mm	Max rope elongation	70.7 mm
x ₂ before tilt compensation	23 mm	x ₂ after tilt compensation	37.5 mm
y ₂ before tilt compensation	16 mm	y ₂ after tilt compensation	25 mm

10 Stacking process simulation with a new prototype

10.1. Description of work

In the new simulations, the device has been redesigned with the new features studied, i.e. two reaction wheels have been added along the two orthogonal axes for the reduction of the oscillation and linear actuators for the movement of the gripping hooks. Tilt angle compensation is not enabled. The reaction wheels are simulated using a simple suspended disk. motors and holders are not shown.

the simulation concerns the complete movement of the box from the gripping to the stacking on the second box. the final goal of the simulation is to verify the effective utility of the changes introduced as well as the presentation of a possible flow chart of the operation.

The list of operations performed by the model is shown in the figure 10.1.

The device starts from the initial position, which corresponds to the position above the second box and the length of the ropes to a minimum. The movement of the trolley always takes place when the device is in a position of minimum distance from the trolley, in order to reduce oscillations as much as possible.

When the command signal is sent to the controller, the trolley moves to reach the pre-set coordinates.

As regards the coordinates to be reached, they can be set in different ways: imposed by the human operator, calculated by a camera positioned in the work environment, or an element of a list of possible positions to be controlled.

The precision of the position to be set just needs to be within the field of view of the camera on the device. It will then be the latter to give the more precise coordinates regarding the relative distance and also the altitude and orientation of the box.

Once arrived on the box, the reaction wheel is operated in order to align the device. After sufficient time to stabilize the rotation, the winch makes the device descend just above the box. The proximity sensors mounted on the mobile platform check whether the position is reached; if not, then the actuators move the platform until it reaches the exact position.

A more detailed sequence of the operation is shown in the figure 10.3; at the end of the operation, due to the small weight imbalance, the device shows a little oscillation.

now, the box is brought over the second box. the orientation of the device can be managed by a second chamber facing upwards, taking some points of the trolley as a reference.

Stacking process simulation with a new prototype

Finally, the box is stacked in the position inserted in the controller memory.

During the entire period of the operation, the two reaction wheels are active and try to maintain the correct orientation of the device.

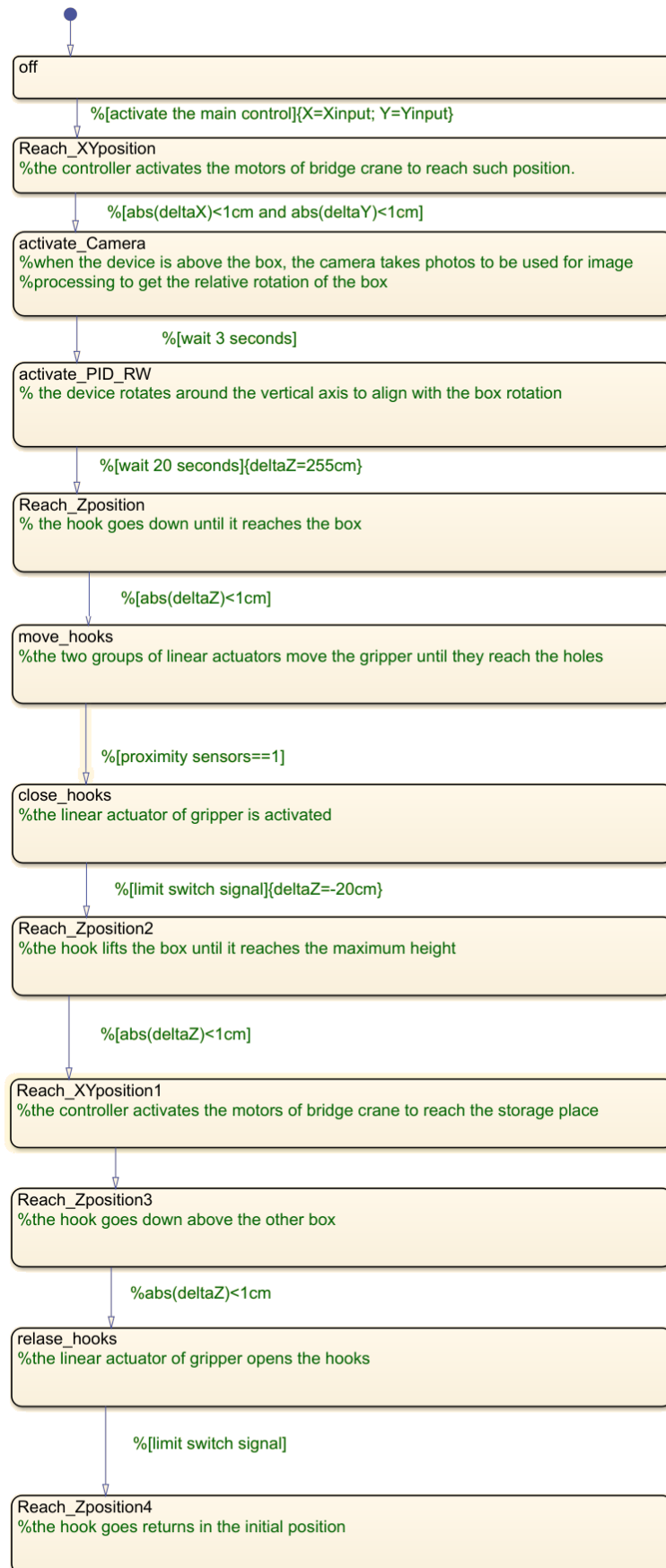


Figure 10. 1: control logic for the gripping and stacking of the box.

Stacking process simulation with a new prototype

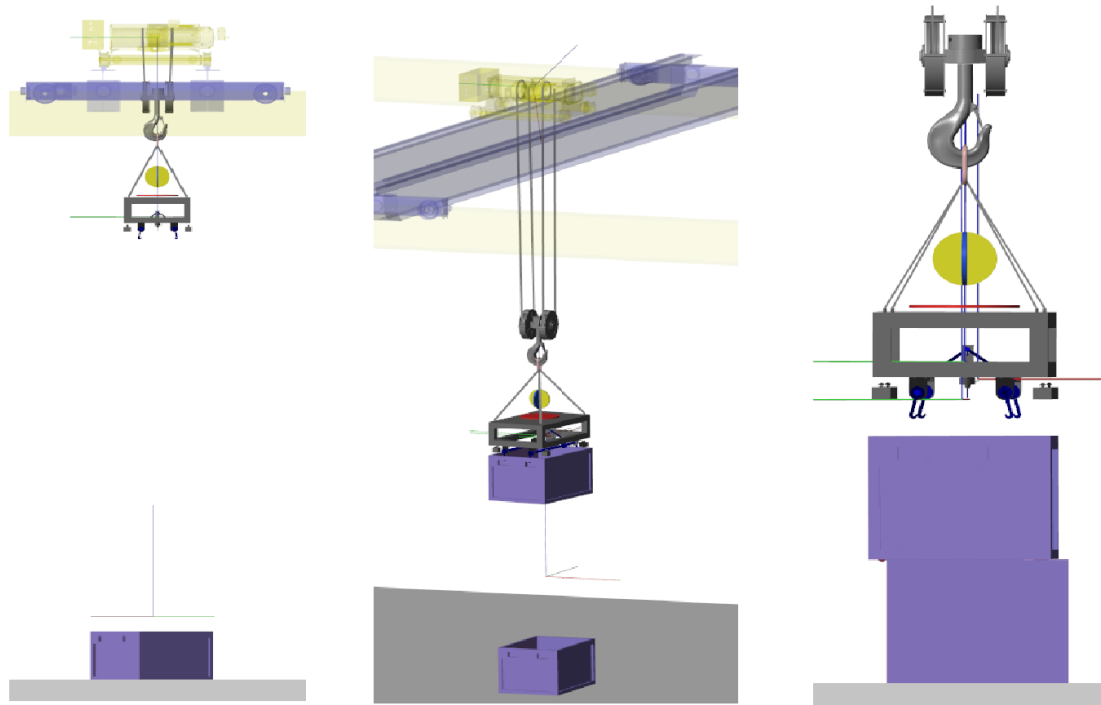


Figure 10. 2. Left: position of the device before the alignment with the box. Centre: box stacking operation. Right: final position of the box.

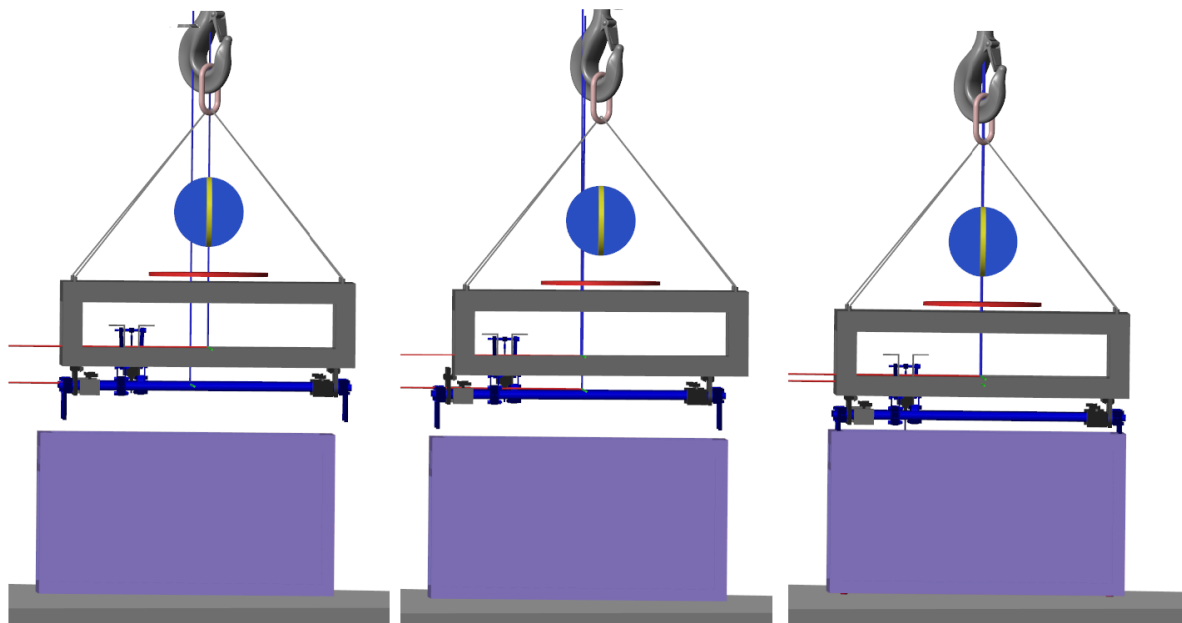


Figure 10. 3: detail of the alignment of the mobile platform containing the gripping mechanism with the holes in the box. Left: starting position. centre: movement of the actuators up to the position reached. right: re-centralization of the device on the box before lifting. the distance between the two blue lines indicates the distance covered (4 cm).

Table 10. 1: parameters for the stacking simulation

LHD mass	20 kg			
LHD inertia	1.3 kg m ²			
Hook mass	13 kg			
KLТ mass	20 kg			
Yaw RW inertia	0.0175 kg m ²			
Hook pulleys diameter	9,5 cm			
Roll and pitch RW Inertia	0.003 kg m ²			
Actuator parameters				
Bridge and trolley max linear speed	25 cm/s	Relative function	Transfer	$\dot{X}, \dot{Y} = \frac{1}{s+1} v_{max}$
Hook max vertical linear speed	14 cm/s	Relative function	Transfer	$\dot{Z} = \frac{1}{0,2s+1} v_{max}$
Linear actuators for alignment system	10 mm/s	Relative function	Transfer	$\dot{x} = \frac{1}{0,1s+1} v_{max}$

10.2. Results

The focus is mainly on the amplitude of oscillation and how the lateral RW work. The other results are commented qualitatively, because the simulation results have no general value because they are obtained from debatable and non-verified data.

The figure shows the absolute position of the device. From it we can discuss the timing of operations: 16 seconds are used for positioning the trolley, 10 seconds for alignment, 25 seconds for descent, 5 seconds for the movement of the mobile hooks.

The diagram of oscillation is useful to understand when the value becomes high. From results it can be deduced that the oscillation becomes high for the Y axis (that corresponds to the direction in which the rigidity of the group is lower) in the descent and ascent phase, due to the small torque caused by the friction between the hook and the two pulleys, and during transport with the payload. Along the X axis, the oscillation is high only when the device rises from the ground, due to the misalignment of the centre of gravity.

The reaction wheels work only with the active component c2 (see paragraph 8.2), because the component c1 caused control problems since the oscillation is not linear anymore due to the four-rope hoist configuration.

The RW work well for the first part of the operations. when the payload weight is added, the system cannot effectively suppress the swing. this means that more torque is required from the motors, or the movement of the trolley must be slower or more controlled.

The general aspect is that the mechanism works well for the hooking phase, while the part of the transport of the load up to the stack presents problems due to the high mass, oscillation of the load.

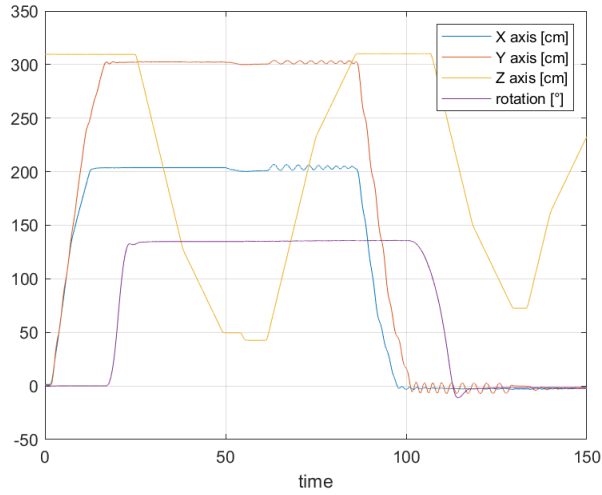


Figure 10. 4: absolute position and rotation of the device

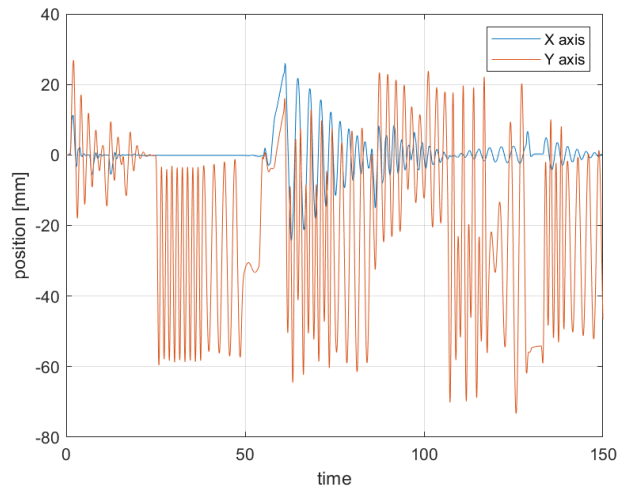


Figure 10. 1: oscillation amplitude respect to the rest position of the device

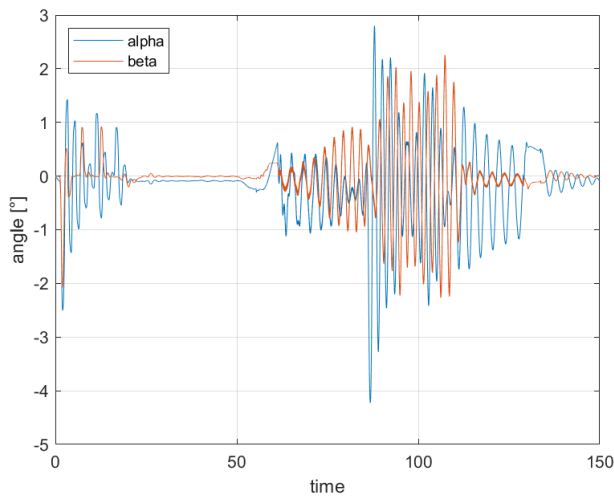


Figure 10. 6: tilting angles measured by the IMU. Alpha and beta are aligned with blue and yellow RW respectively

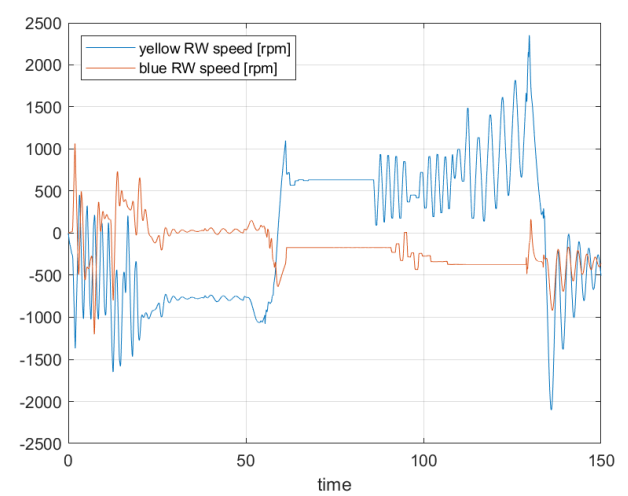


Figure 10. 7: speed of two reaction wheels during the work. The yellow and blue RW is initially aligned with the Y and X axes respectively.

11 Conclusion and outlook

11.1. Results discussion

The use of the reaction wheel is a valid method to allow the rotation of the LHD. The positioning accuracy depends above all on the non-linearity of the friction in the thrust bearing and the dynamic response of the actuator.

For the limitation of lateral oscillations, it has been found that the use of reaction wheels with axis oriented in the direction of the oscillations requires very high motor torque output to be used as the only damping system. The best way is to combine the trolley speed control to roughly limit the oscillations (for example using an input shaping control) and the reaction wheel for a fine adjustment.

If single chain hoists are used, RW are not very effective. Their use could be more appreciated if multiple rope hoists are used, especially in the case of fairly wide spreaders (i.e. the ropes are spaced from each other) because in this case the primary oscillation is reduced, while the secondary oscillation (tilting) becomes more important. In this case, therefore, RW act directly in the direction of the oscillation. The secondary oscillation has a higher natural frequency than the primary one, for this reason the dynamic response of the motor must be high and without delay.

Passive gyroscopic phenomena (created by the high speed of the yaw movement reaction wheel) can be useful in case one oscillation axis is much more rigid than the other, in order to transfer the energy from one direction to the other orthogonal direction.

Active use of the gyroscopes (i.e. the control of the gimbal axis of the gyroscope) are obtained by coupling two gyroscopes rotating in the opposite direction, having a resultant zero angular momentum. This system, in the literature known as the scissored-pair control moment gyroscope, is already used in aerospace. In the thesis it was not addressed with a simulated model due to lack of time.

The advantages of using the gyroscopic system with respect to the reaction wheels lies in the fact that the use of the former provides higher torque for the same mass and energy input. The disadvantage lies in the greater complexity of construction and control.

In chapter 9 construction designs were investigated to increase positioning accuracy and tilt compensation. Different solutions have been presented for the insertion of rigid actuators or pulley mechanisms in the device which allow very precise movements in a short range. The simulation of the dynamics on Matlab confirmed their theoretical functioning. A thorough structural analysis or construction of prototypes will give more information on the choice of one design over another in terms of structural rigidity, costs, complexity, dimensions.

A further important point in the thesis was the discussion of a possible workflow for the stacking process, described in chapter 10.

The discussion was theoretical and is susceptible to errors since no operations have been tested. It is useful as a starting point for future works. The crucial point that must be developed is the implementation of the automatic control of the bridge crane motors, such as voltage and frequency control.

A study on the accuracy and repeatability of positioning of the trolley must be done to obtain data on the position interval that the LHD must be able to cover with the integrated mechanism.

A new idea presented is to add proximity or contact sensors as an additional LKT detection sensor. Since they are inexpensive and reliable, they can be used to ensure that the LHD is in the exact position for gripping.

Another issue to investigate is how to ensure the positioning accuracy of the box during stacking. since the LHD camera is out of order when the KLT is taken, it is conceivable to install a series of external cameras that have visibility into the operations in progress. Since such a system would require a high number of cameras, or a sufficient position resolution is not achieved, another way is to record the positions that each box to be stacked must have at the end of the process (taking into account the dimensions, height, etc) and use the cameras as a feedback sensor together with the overhead crane absolute encoders.

11.2. Prospect of use

The advantages of using this device over other systems are now discussed.

The main advantage of this device is that it can be easily assembled on a pre-existing crane. This reduces the installation costs of new infrastructures. Floor storage is permissible in any place within the crane operating range, which can be very large, and can be transferred without any problem. An example in which it might be advantageous to introduce this system is when box loading and storage take place on floors with a high difference in altitude, thus allowing the winch to be exploited.

The main disadvantage lies in the fact that only one box can be taken at a time, the speed of movement is very low, and the dead weight (weight of the bridge, trolley, hook, and device) is high. The disadvantages described are mainly present in the case of storage of small boxes. These disadvantages are considerably reduced if storage takes place for heavy elements, such as pallet cages.

Pallet cages are standardized in the sizes 800x600 or 1200x800 mm with a maximum load between 400 and 1000 kg. New gripping systems must be specifically designed. For

example, in the system studied in the KraaS project (Bolender, et al. 2018) side hooks are used inserting them under the upper part of the pallet cage.

As regards the scalability of the components, oversizing the reaction wheel for the yaw movement is feasible. In fact, considering negligible the friction force, the size of the wheel is proportional to the maximum speed of the device. Saturating the engine speed (3000 rpm) it is possible to have a relatively small wheel size. And also, the motor torque is low, not needing to counteract other forces except the inertia force of the LHD and payload.

having a much larger mass of the load, the crane motors must accelerate the device with greater precision to avoid considerable oscillations. the lateral reaction wheels (as also for the pair of gyroscopes) can be considered valid to eliminate secondary oscillations of small intensity.

the relative displacements of linear actuators can be effectively used only for the compensation of the inclination angle and very small displacements since the considered LHD should have a mass that is much less than the mass of the pallet cage.



Figure 11.1. left: pallet cage Magnum Optimum with dimensions 1200x800x958 mm, net weight 50kg and maximum load 750 kg. right: pallet cages floor storage (web source: schoellerallibert.com)

An interesting field of application of all the features studied in the thesis is cable-suspended parallel robot systems. Instead of using crane bridges, that necessarily have high mass respect to the KLT, a system of pulleys moved by external motors fixed on the ground lifts and stacks the boxes. Such system can consistently reduce the masses involved. All the applications about reaction wheels and counterweight systems could be considered for stabilisation and balance of the box. References for the control of cable-suspended robots can be found in (Zi e Qian 2017).

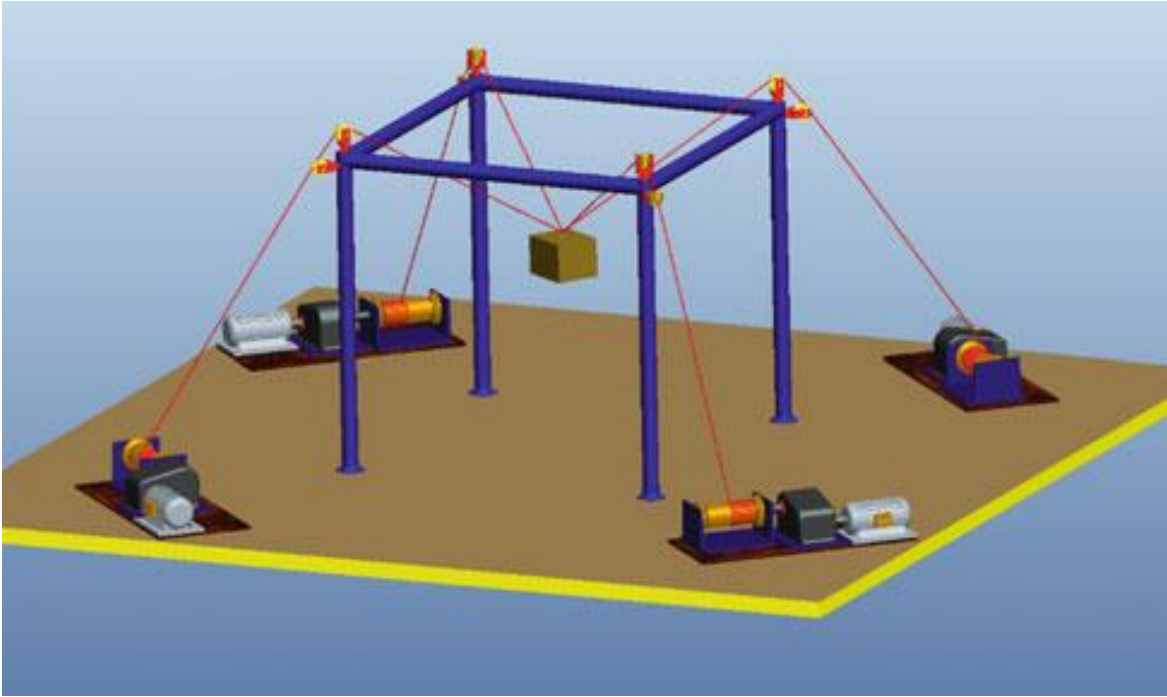


Figure 11. 2: example of cable-suspended parallel robot application that can be used for KLT storage (Zi e Qian 2017)

bibliography

- AGV market insights*. 2019. <https://www.prmitteilung.de/2019/06/22/automated-guided-vehicle-agv-market-insights-forecast-2025> (accessed May 2020).
- Aranovskiy, Stanislav, Igor Ryadchikov, Evgeny Nikulchev, Jian Wang, e Dmitry Sokolov. «Experimental Comparison of Velocity Observers: A Scissored Pair Control Moment Gyroscope Case Study.» *IEEE Access*, 2020: 21694–21702.
- Benzaouia, Abdellah, Fouad Mesquine, e Mohamed Benhayoun. *Saturated Control of Linear Systems*. Vol. 124. Cham: Springer International Publishing, 2018.
- Bolender, Steffen, Jan Oellerich, Meike Braun, Markus Golder, e Kai Furmans. «System zur reproduzierbaren, automatischen und sicheren Stapelung von Gitterboxen mit einem Brückenkran – KrasS.» 2018. 6.
- Brogliato, Bernard, Rogelio Lozano, Bernhard Maschke, e Olav Egeland. *Dissipative Systems Analysis and Control*. Cham: Springer International Publishing, 2020.
- Chan, Tze Fun, and Keli Shi. *Applied intelligent control of induction motor drives*. Hoboken N.J.: Wiley, 2011.
- Chiu, Jimmy, and Ambarish Goswami. *Design of a Wearable Scissored-Pair Control Moment Gyroscope (SP-CMG) for Human Balance Assist*. Buffalo, New York, USA: International Design Engineering Technical Conferences and Computers and Information in Engineering Conference, 2014.
- Dianwei, Qian. *anti-sway control for cranes*. Berlin, Boston: De Gruyter, 2018.
- Elmenreich, Wilfried. *Sensor Fusion in Time-Triggered Systems*. Dissertation. Technischen Universität Wien. Institut für Technische Informatik, 2002.
- Fischer, Raphael. *Entwicklung und Konstruktion eines Lastaufnahmemittels mit automatischer Orientierung am einsträngigen Tragmittel*. Masterarbeit. Karlsruher Institut für Technologie. Institut für Fördertechnik und Logistiksysteme, 2019.
- Gajjar, Manish J. *Mobile Sensors and Context-Aware Computing*. Cambridge, MA: Morgan Kaufmann, 2017.
- Gasparetto, Alessandro, e Marco Ceccarelli. *Mechanism Design for Robotics*. Vol. 66. Cham: Springer International Publishing, 2019.
- Herz, Leonard. *Dimensionierung und Implementierung der Regelung eines Lastaufnahmemittels für automatisierte Brückenkrane*. Abschlussarbeit. Karlsruher Institut für Technologie. Institut für Fördertechnik und Logistiksysteme, 2020.
- Hong, Keum-Shik, and Umer Hameed Shah. *Dynamics and Control of Industrial Cranes*. Singapore: Springer Singapore, 2019.
- Koether, Reinhard. *Distributionslogistik*. Wiesbaden: Springer Fachmedien Wiesbaden, 2018.
- Lacarbonara, Walter, Balakumar Balachandran, Jun Ma, J. A. Tenreiro Machado, e Gabor Stepan. *Nonlinear Dynamics of Structures, Systems and Devices*. Cham: Springer International Publishing, 2020.
- Martin, Heinrich. *Transport- und Lagerlogistik*. Wiesbaden: Springer Fachmedien Wiesbaden, 2016.

- Mathworks products*. n.d. <https://www.mathworks.com/products.html> (accessed May 2020).
- Matt, Dominik T., Vladimír Modrák, e Helmut Zsifkovits. *Industry 4.0 for SMEs*. Cham: Springer International Publishing, 2020.
- naicranes*. n.d. <http://www.naicranes.com/dev/cranes/hoists.htm> (accessed May 2020).
- O', W. Connor, e H. Habibi. «Gantry crane control of a double-pendulum, distributed-mass load, using mechanical wave concepts.» *Mechanical Sciences*, 2013: 251–261.
- Rauscher, Florentin, Samuel Nann, and Oliver Sawodny. “Motion Control of an Overhead Crane Using a Wireless Hook Mounted IMU.” 5677–5682. IEEE, 2018.
- Seifert, Jonas. *Entwicklung und Konstruktion eines Modells zur Lageausrichtung von Lastaufnahmemitteln automatisierter Brückenkrane mittels Reaktionsrädern*. Masterarbeit. Karlsruher Institut für Technologie. Institut für Fördertechnik und Logistiksysteme, 2019.
- Simón Mata, Antonio, et al. *Fundamentals of Machine Theory and Mechanisms*. Vol. 40. Cham: Springer International Publishing, 2016.
- Wen, Haoran. *Toward Inertial-Navigation-on-Chip*. Cham: Springer International Publishing, 2019.
- Yang, Yiping. «Numerical Methods for the inverse dynamics simulation of underactuated mechanical systems.» s.d.
- Youngjoo, Kim, and Bang Hyochoong. *Introduction to Kalman Filter and Its Applications*. 2018. <https://www.intechopen.com/books/introduction-and-implementations-of-the-kalman-filter/introduction-to-kalman-filter-and-its-applications>.
- Zerrik, El Hassan, Said Melliani, e Oscar Castillo. *Recent Advances in Modeling, Analysis and Systems Control: Theoretical Aspects and Applications*. Vol. 243. Cham: Springer International Publishing, 2020.
- Zi, Bin, e Sen Qian. *Design, Analysis and Control of Cable-suspended Parallel Robots and Its Applications*. Singapore: Springer Singapore, 2017.